ORIGINAL ARTICLE

An evaluation of tropical waves and wave forcing of the QBO in the QBOi models

Laura A. Holt[1*] | François Lott[2] | Rolando R. Garcia[3] | George N. Kiladis[4] | Yuan-Ming Cheng[4] | James A. Anstey[5] | Peter Braesicke[6] | Andrew C. Bushell[7] | Neal Butchart[8] | Chiara Cagnazzo[9] | Chih-Chieh Chen[3] | Hye-Yeong Chun[10] | Yoshio Kawatani[11] | Tobias Kerzenmacher[6] | Young-Ha Kim[12] | Charles McLandress[5, 13] | Hiroaki Naoe[14] | Scott Osprey[15] | Jadwiga H. Richter[3] | Adam A. Scaife[8, 16] | John Scinocca[5] | Federico Serva[9] | Stefan Versick[6] | Shingo Watanabe[11] | Kohei Yoshida[14] | Seiji Yukimoto[14]

This is the author manuscript accepted for publication and has undergone full peer rev
has not been through the copyediting, typesetting, pagination and proofreading process
may lead to differences between this version and the Version of Record. Please cite this
as doi: 10.1002/qj.3827

[1]NorthWest Research Associates, Boulder, Colorado

[2]Laboratoire de Météorologie Dynamique, Ecole Normale Supérieure, Paris, France

[3]National Center for Atmospheric Research, Boulder, Colorado

[4]Physical Sciences Division, NOAA/Earth System Research Laboratory, Boulder, Colorado

[5]Canadian Centre for Climate Modelling and Analysis (CCCma), Victoria, Canada

[6]Karlsruher Institut für Technologie (KIT), Karlsruhe, Germany

[7]Met Office, Exeter, UK

[8]Met Office Hadley Centre (MOHC), Exeter, UK

[9]Institute of Marine Sciences, National Research Council (ISMAR-CNR), Rome, Italy

[10]Yonsei University, Seoul, South Korea

[11]Japan Agency for Marine-Earth Science and Technology (JAMSTEC), Yokohama, Japan

[12]Ewha Womans University, Seoul, South Korea

[13]University of Toronto, Toronto, Canada

[14]Meteorological Research Institute (MRI), Tsukuba, Japan

[15]National Centre for Atmospheric Science (NCAS), University of Oxford, Oxford, UK

[16]University of Exeter, Exeter, UK

Correspondence
Laura A. Holt, NorthWest Research Associates, 3380 Mitchell Lane, Boulder, CO 80301, USA
Email: laura@nwra.com

Funding information
See acknowledgments.

We analyze the stratospheric waves in models participating in phase 1 of the Stratosphere–troposphere Processes And their Role in Climate (SPARC) Quasi-Biennial Oscillation initiative (QBOi). All models have robust Kelvin and mixed Rossby-gravity wave modes in winds and temperatures at 50 hPa and represent them better than most of the Coupled Model Intercomparison Project Phase 5 (CMIP5) models. There is still some spread among the models, especially concerning the mixed Rossby-gravity waves. We attribute the variability in equatorial waves among the QBOi models in part to the varying horizontal and vertical resolutions, to systematic biases in zonal winds, and to the considerable variability in convectively coupled waves in the troposphere among the models: only roughly half of the QBOi models have realistic convectively coupled Kelvin waves and only a few models have convectively coupled mixed Rossby-gravity waves. The models with stronger convectively coupled waves tend to produce larger zonal mean forcing due to resolved waves in the QBO region. Finally we evaluate the Eliassen-Palm (EP) flux and EP flux divergence of the resolved waves in the QBOi models. We find that there is a large spread in the forcing from resolved waves in the QBO region, and the resolved wave forcing has a robust correlation with model vertical resolution.

KEYWORDS
quasi-biennial oscillation, equatorial waves, wave-mean flow interaction

1 | INTRODUCTION

The quasi-biennial oscillation (QBO) in equatorial lower-stratosphere zonal mean winds is a result of wave-mean flow interaction between mean winds and tropical Kelvin, mixed Rossby-gravity, inertia-gravity, and small-scale gravity waves (e.g. Lindzen and Holton, 1968; Holton and Lindzen, 1972; Dunkerton, 1997; Baldwin et al., 2001). The precise partitioning of these various waves in the forcing of the QBO is still an area of active research. Observational constraints on the contributions of various waves to the forcing of the QBO remain elusive for multiple reasons: (1) waves are highly

variable in both space and time; (2) each observational technique can only measure a portion of the wave spectrum; (3) estimates of momentum flux derived from observations rely on many assumptions, which results in large uncertainties in the estimated flux. Geller et al. (2013) showed that while global spatial and temporal patterns of gravity wave absolute momentum fluxes are similar in observations and high-resolution models, the magnitudes of the absolute momentum fluxes derived from observations have large uncertainties. Global high-resolution modeling studies suggest that tropical Kelvin waves provide approximately half of the eastward forcing for the QBO in eastward shear zones (e.g. Kawatani et al., 2010; Holt et al., 2016). The rest of the eastward forcing in these studies was provided by small-scale gravity waves, and in westward shear zones the majority of the westward forcing was provided by small-scale gravity waves. Estimates based on observations also suggest that a large portion of the forcing for the QBO is provided by small-scale gravity waves (e.g. Sato and Dunkerton, 1997; Ern and Preusse, 2009; Alexander and Ortland, 2010; Ern et al., 2014).

Regardless of the uncertainties in the contribution of the various equatorial waves to the driving of the QBO, some atmospheric general circulation models (GCMs) have been able to obtain a QBO-like oscillation with various tunings of different model parameters, some without nonorographic gravity wave parameterizations (e.g., Takahashi, 1996; Horinouchi and Yoden, 1998; Hamilton et al., 1999; Watanabe et al., 2008; Kawatani et al., 2010) and some with this forcing (e.g., Scaife et al., 2002; Giorgetta et al., 2006; Kim and Chun, 2015). GCMs run at resolutions typical of climate models must rely on nonorographic gravity wave parameterizations to provide the small-scale gravity wave forcing required for the QBO, and this provides by far the largest tuning parameter for obtaining a realistic model QBO (e.g., Scaife et al., 2000; Giorgetta et al., 2002; Richter et al., 2014; Schirber et al., 2014). Some of the other model parameters that affect the simulated equatorial waves and model QBO-like oscillations are horizontal resolution (Holt et al., 2016), vertical resolution (Boville and Randel, 1992; Anstey et al., 2016), horizontal diffusion (Scaife et al., 2002), model lid placement (Lawrence, 2001; Osprey et al., 2013), and even the choice of dynamical core (Yao and Jablonowski, 2015). Since there seems to be many different parameters that affect the model QBO-like oscillation, it is important to understand the sensitivity of the modeled QBO-like oscillation to model configuration.

The Stratosphere–troposphere Processes And their Role in Climate (SPARC) Quasi-Biennial Oscillation initiative (QBOi) (Butchart et al., 2018) provides an opportunity to systematically look at the relationship between various model parameters and the simulated QBO-like oscillations in many different climate models. Phase 1 of the QBOi consists of five experiments that were designed to (i) evaluate the ability of GCMs to produce a realistic QBO-like oscillation under present-day conditions, (ii) determine the robustness in the simulated responses to imposed climate forcing scenarios, and (iii) examine model influence on QBO predictability (Butchart et al., 2018). In all, 17 GCMs participated in the QBOi in some or all of the experiments. In this paper, we evaluate equatorial waves and wave forcing of the QBO in models participating in Experiment 1.

This paper is organized as follows. In Section 2 we briefly describe the relevant experiments in the participating QBOi models. In Section 3 we evaluate the model precipitation spectra. In Section 4 we evaluate Kelvin and mixed Rossby-gravity waves in equatorial winds and temperatures. In Section 5 we analyze EP flux and EP flux divergence in the QBO region with respect to various model parameters and tropospheric and stratospheric equatorial waves. Finally, we provide a summary and closing remarks in Section 6.

2 | MODELS AND EXPERIMENT DESIGN

We evaluate equatorial Kelvin and mixed Rossby-gravity (MRG) waves in the precipitation, winds, and temperature in the models participating in the QBOi that performed Experiment 1. For a detailed description of the participating models, we refer the reader to Butchart et al. (2018). Briefly, for Experiment 1 each participating model completed

TABLE 1 Models participating in Experiment 1 of the QBOi. Based on Tables 5 and 6 and Figure 5 in Butchart et al. (2018). Vertical gridspacing (Δz) is given for altitudes between approximately 10 and 25 km. When Δz is not constant in altitude, the range of vertical gridspacing is given.

Model	Horiz. resolution	Δz (10-25 km)	References
60LCAM5	100 km	500-800 m	Richter et al. (2014)
AGCM3-CMAM	T47	500 m	Scinocca et al. (2008); Anstey et al. (2016)
CESM1(WACCM5-110L)	1.25° × 0.94°	500 m	Garcia and Richter (2019)
ECHAM5sh	T63	600-700 m	Manzini et al. (2012); Serva et al. (2018)
EMAC	T42	600-700 m	Jöckel et al. (2005, 2010)
HadGEM2-A	1.875° × 1.25°	1-1.2 km	The HadGEM2 Dev. Team (2011)
HadGEM2-AC	1.875° × 1.25°	1-1.2 km	Kim and Chun (2015); The HadGEM2 Dev. Team (2011)
LMDz6	2.5° × 1.25°	0.9-1.1 km	Lott et al. (2005, 2012)
MIROC-AGCM-LL	T106	550 m	Kawatani et al. (2011)
MIROC-ESM	T42	680 m	Watanabe et al. (2011)
MRI-ESM2	T159	500-700 m	Yukimoto et al. (2012); Adachi et al. (2013)
UMGA7	1.875° × 1.25°	600-800 m	Walters et al. (2017)
UMGA7gws	1.875° × 1.25°	600-800 m	Bushell et al. (2015); Walters et al. (2017)

a one- to three-member ensemble of 30-year simulations using observed sea surface temperatures and sea ice from 1 January 1979 to 28 February 2009. Experiment 1 is modeled after the Coupled Model Intercomparison Project Phase 5 (CMIP5) experiment 3.3 (the Atmospheric Model Intercomparison Project (AMIP) (Taylor et al., 2012)). The participating models are listed in Table 1.

3 | TROPICAL PRECIPITATION SPECTRA

Latent heat release in precipitating clouds is the primary source of vertically propagating stratospheric equatorial waves (SEWs) that drive the QBO (e.g., Holton, 1972; Salby and Garcia, 1987; Garcia and Salby, 1987; Ricciardulli and Garcia, 2000; Stephan and Alexander, 2015). Tropical cloudiness and precipitation also tend to organize into preferred equatorial wave modes (Takayabu, 1994; Wheeler and Kiladis, 1999; Cho et al., 2004), and the dispersion characteristics and structure of these convectively coupled equatorial waves (CCEWs) resemble those of the dry SEWs predicted by linear theory (Kiladis et al., 2009). SEWs and CCEWs are at least partly related, which is evidenced by the fact that SEWs are often observed above CCEWs (e.g., Maury et al., 2013). However, the relationship between CCEWs and SEWs is not straightforward, and substantial SEWs can be generated even when the convection is not organized (Garcia and Salby, 1987; Salby and Garcia, 1987). Furthermore, the coherencies between CCEWs and SEWs diminish with increasing altitude (Hendon and Wheeler, 2008), and temporal variations of Kelvin wave activity in the tropical tropopause layer

(TTL) and the stratosphere tend to follow changes in propagation conditions instead of changes in Kelvin wave activity in convection (Alexander and Ortland, 2010; Flannaghan and Fueglistaler, 2013). In this section we focus on evaluating the ability of the QBOi models to reproduce the observed convection and CCEWs.

The model convective parameterization scheme has a large influence on the generation of SEWs that drive the QBO (Horinouchi et al., 2003). To evaluate the convective parameterization in the QBOi models, we focused on precipitation and followed the method described in Wheeler and Kiladis (1999) to produce background precipitation spectra as well as the symmetric and antisymmetric components with respect to the equator, which reveal the CCEW modes (Matsuno, 1966; Kiladis et al., 2009; Garfinkel et al., 2017; Paldor et al., 2018). We used 10 years of daily mean precipitation with a 96-day window and 65-day overlap, which resulted in 114 windows over the 10-year period. The zonal and temporal means were subtracted from each window and tapered in time before computing the fast Fourier transform. After the fast Fourier transform was computed for each time window, the spectra obtained from each of the 114 96-day windows were averaged in time and in latitude from 10°S–10°N.

Figure 1 shows the raw precipitation power spectra as a function of zonal wavenumber and frequency in cycles per day (cpd) for the QBOi models and the Global Precipitation Climatology Project (GPCP). HadGEM2-AC and UMGA7gws are virtually indistinguishable from HadGEM2-A and UMGA7, respectively, and are therefore not included in Figure 1 (as well as Figures 2–5 and Figures 7–10, for the same reason). As in previous studies that examined suites of climate models (e.g., Horinouchi et al., 2003; Lin et al., 2006; Lott et al., 2014), there is a large spread among models in their ability to simulate a realistic precipitation spectrum. As shown previously for observations from the Tropical Rainfall Measuring Mission (Kim and Alexander, 2013), GPCP precipitation reveals a red spectrum that organizes strongly along the -20 m s^{-1} and 15 m s^{-1} phase speed lines and has slightly more power at the westward zonal wavenumbers. For westward waves this organization is not as tightly organized as it is for the eastward waves, but at least for frequencies greater than 0.2 cpd it organizes close to the -20 m s^{-1} line. All of the models show the preference for westward propagating waves seen in GPCP to some degree. All of the models also organize to some degree along the 15 m s^{-1} phase speed line for eastward propagating waves, but almost all of the models organize along phase speeds that are slower than GPCP for westward propagating waves. 60LCAM5 and CESM1(WACCM-110L) appear to have the best representation of tropical precipitation.

The symmetric and antisymmetric components of the spectrum reveal the organization of tropical precipitation into preferred modes. Again as in Wheeler and Kiladis (1999), we decomposed the precipitation spectra, $P(\phi)$, into symmetric and antisymmetric anomalies with respect to the equator:

$$P(\phi)_{symm} = [P(\phi) + P(-\phi)]/2 \quad (1)$$

$$P(\phi)_{asym} = [P(\phi) - P(-\phi)]/2 \quad (2)$$

where ϕ is latitude. As in previous studies, we exclude the equator and latitudes directly adjacent to the equator in the analysis (e.g., Hendon and Wheeler, 2008; Wheeler and Kiladis, 1999). This is a compromise between the best representation of the Kelvin modes, which peak at the equator, and the MRG modes, which peak off of the equator. Figure 2 shows the symmetric component of the precipitation spectra divided by the background spectra, and Figure 3 shows the antisymmetric component of the precipitation spectra divided by the background spectra (note the reduced wavenumber range compared to Figure 1). The background spectra were obtained by smoothing the raw spectra in Figure 1 with a 1-2-1 smoothing in frequency and wavenumber as described in Wheeler and Kiladis (1999). Dispersion

curves for leading equatorial modes of variability (Matsuno, 1966; Garfinkel et al., 2017) are superimposed on the plots using equivalent depths of 12, 25, and 50 m. Ratios higher than 1.1 are where the spectral power is significantly higher than the background and can be interpreted as organized convection (Wheeler and Kiladis, 1999). The organization of convection along the dispersion curves of theoretical equatorial modes implies coupling between these waves and convection. Such waves are referred to as CCEWs. In Figure 2 there is a large spread in the CCEWs in the QBOi models, but most of the models do show at least some organization around the preferred equatorial modes in GPCP for eastward propagating Kelvin waves. In general the models have smaller ratios than GPCP, indicating lower degrees of organization in the models than in the observed precipitation. The models that have the most realistic organization are the models that have the most realistic raw precipitation spectra with the best organization around the 15 m s^{-1} phase speed line (the 15 m s^{-1} phase speed line in Figure 1 is essentially the 25 m equivalent depth curve in Figure 2). In addition, we note that almost all of the models have some Madden-Julian Oscillation (MJO)-like signal (frequency less than 1/30 cpd and wavenumber 1–5).

For the antisymmetric component of the spectra in Figure 3, about half of the models exhibit some organization along the dispersion curves for the MRG modes (Matsuno, 1966; Paldor et al., 2018) as seen in GPCP. GPCP has a well defined peak centered around the 25 m equivalent depth contour, indicating that MRGs organize a significant portion of the precipitation variability, along with eastward propagating inertio-gravity waves (EIGs, Kiladis et al., 2016). None of the models shows this level of organization, although 60LCAM5 comes close and CESM1(WACCM-110L), MIROC-ESM, and ECHAM5sh have a moderate level of organization of both MRGs and EIGs as well. Like symmetric spectra in Figure 2, the models that have organization that best matches the organization in GPCP are the models that have the most realistic raw precipitation spectra in Figure 1.

To summarize, the QBOi models vary widely in their ability to simulate the overall variability in precipitation and also in their ability to simulate convectively coupled waves, which is consistent with previous model comparisons (e.g., Horinouchi et al., 2003; Lin et al., 2006; Straub et al., 2010; Lott et al., 2014).

4 | KELVIN AND MRG WAVES IN EQUATORIAL WINDS

To analyze the Kelvin and MRG waves in equatorial winds, we analyze the spectra of zonal and meridional winds in the QBOi models and compare them to those from the European Centre for Medium-Range Weather Forecasts Interim Reanalysis (ERAI) (Dee et al., 2011). We chose ERAI simply for convenience, but the choice of reanalysis dataset should not make a difference in the results. For example, Kim et al. (2019) showed that the spectrum of zonal and meridional winds at 50 hPa is very similar among several reanalyses. To produce the spectrum of zonal and meridional winds, we first tapered the zonal and meridional wind fields by a cosine function centered at the equator and crossing the zero line at ±10° and then averaged over the latitudinal band (10°S–10°N). We applied the cosine taper to the zonal wind to extract the Kelvin waves and to the meridional wind to extract the MRG waves since the zonal wind is expected to be symmetric about the equator for Kelvin waves and the meridional wind is expected to be symmetric about the equator for MRG waves.

The spectra for the zonal wind at 50 hPa are shown in Figure 4 as a function of zonal wavenumber and frequency in a log-log format. To preserve variance, each spectrum is multiplied by frequency and wavenumber. This method of plotting the spectra has the advantage of giving the energy of the signal since it does not require removing the background. Figure 4 shows that all of the QBOi models have substantial power with well defined maxima in both the eastward and westward directions. In the westward direction, we know from Lott et al. (2009) that a substantial portion of the signal is due to free planetary waves that originate from outside of the tropics. In the eastward direction, all

models have strong signatures of Kelvin waves often exceeding the reanalysis, even models with little or no convectively coupled Kelvin waves (CCKWs). That the Kelvin waves in the QBOi models are stronger than the reanalysis could be in part because most of the QBOi models have an eastward bias in the lower stratosphere (see Bushell et al. (2019), part of this Special Section). This is consistent with the same results from CMIP5 models in Lott et al. (2014), where the models with a QBO showed significantly larger Kelvin waves than the others. In general, models that have the strongest signatures of Kelvin waves in Figure 4 also have the strongest signatures of CCKWs in Figure 2. However the Kelvin wave signal in Figure 4 is shifted to longer equivalent depth than in Figure 2. This is due to the fact that faster waves have longer vertical wavelengths and are therefore less filtered by dissipative processes that are enhanced near critical levels, where the phase velocity of the waves approaches that of the background wind. This filtering decorrelates the waves in the stratosphere from the convectively-coupled waves at lower levels.

Although most models that have the strongest convectively coupled waves also have strong stratospheric waves, there is one notable exception: the 60LCAM model almost has the strongest convectively coupled waves in Figure 2j and almost the smallest Kelvin wave signal in Figure 4j (although in both figures 60LCAM compares well to both GPCP and ERAI). We attribute this difference to the fact that this model has a systematic eastward zonal mean zonal wind bias at 70 hPa (see Figure 1 in Bushell et al. (2019), part of this Special Section). This induces filtering for the eastward waves, illustrating again how the mean wind can drastically enhance attenuation of the tropospheric signal. Another reason that 60LCAM has strong CCKWs and weaker stratospheric Kelvin waves compared to other models could be vertical resolution. It is interesting that 60LCAM has the largest difference between tropospheric and stratospheric vertical resolution (less than 0.5 km between 10–15 km and nearly 0.8 km between 20–25 km; see Figure 5 in Butchart et al. (2018)). This will be discussed again in Section 5.2.

Figure 5 shows spectra for meridional winds at the equator at 50 hPa as a function of wavenumber and frequency. Whereas few models showed substantial organization into MRG wave modes in Figure 3, in Figure 5 all of the QBOi models have power in the westward direction with maxima near the dispersion curves for MRG waves as seen in ERAI. Some models also have some EIG power, although this is lacking in ERAI. Note also that the MRG signal is shifted to larger equivalent depth, or horizontal phase speed, compared to the convectively coupled waves, again consistent with filtering. As with zonal wind spectra, many of the models have maxima in power that are substantially higher than seen in ERAI. The models with the strongest signals (MIROC-AGCM-LL, MIROC-ESM, ECHAM5sh, CESM1(WACCM-110L), and 60LCAM5) are also the models that show the most organization of precipitation variability into MRG modes. A good illustration is 60LCAM5, which has the largest convectively coupled wave signal and the largest stratospheric MRG signal. This strong troposphere-stratosphere relation is probably favored by the eastward zonal mean zonal wind bias that was detrimental to the 60LCAM5 Kelvin waves in Figure 4 since this bias induces filtering for the eastward propagating waves and not for westward propagating waves.

To characterize the spatial structure and the life cycle of the stratospheric equatorial waves we performed a composite analysis of bandpass filtered fields as in Lott et al. (2014). The bandpass filter operates in the frequency-wavenumber Fourier space and is shown in Figure 6 for MRG waves on the left and Kelvin waves on the right. The bandpass filter shown in Figure 6 is applied to the spectra in Figures 4 and 5. Example spectra from ERAI at 50 hPa are shown in 6. The left panel shows the westward part of meridional wind (v) symmetric spectrum and the right panel shows the eastward part of zonal wind (u) symmetric spectrum. The filter largely contains the broadband spectral maxima associated with Kelvin and MRG waves in ERAI, which guarantees that the filtered fields include them as well. After the spectra are filtered by the bandpass filter in wavenumber-frequency space, we return to physical space.

To diagnose when a Kelvin wave is present at 50 hPa, we evaluate an index whose value equals the maximum of the filtered zonal wind averaged in latitude between 10°S and 10°N, and identify the longitude, λ_M, at which this maximum occurs. The composites are centered on λ_M and built from averages over dates when maxima of this index exceed a

given threshold. In each dataset the threshold is chosen so that around 30 events are selected, and the length of each dataset for both the models and reanalysis is the same. We select a relatively small number of events to guarantee independence among the selected wave packets, keeping in mind that each wave packet can have a life cycle that lasts near a month. Since this number is rather small, we have verified that none of our results are affected by moderate changes in the thresholds, provided that about the same number of dates are selected in each model (not shown). For the MRG waves, we follow the same procedure but use the meridional wind, v, to define the index.

Figure 7 shows longitude-time composites of the zonal wind anomaly at the equator. All of the QBOi models simulate substantial eastward propagating disturbances with wind maxima often exceeding 5 m s^{-1}. Several of the QBOi models have much larger wind anomalies than ERAI. The models with the largest wind anomalies tend to be the models with the strongest CCKW signatures. Note here the rather large values in the 60LCAM5 composite, apparently contradicting the spectra in Fig. 4. This highlights the fact that the composite does not consider all dates but averages the 30 largest wave events. Compared to the same results from CMIP5 in Lott et al. (2014) there is less spread among models in phase speed.

Figure 8 shows longitude-latitude composites of temperature anomalies with horizontal wind vectors at 0-day lag. These confirm that the composites in Figure 7 are indeed showing Kelvin waves, since the disturbance horizontal wind is zonal and in quadrature with the temperature. The signal in temperature is also quite substantial, reaching more than 3K. Again the magnitude of the temperature anomalies in many of the QBOi models exceeds the magnitude of the temperature anomaly in ERAI.

Figure 9 shows longitude-time composites of the meridional wind anomaly at the equator. All of the QBOi models simulate westward propagating disturbances that shift continuously toward the east, consistent with westward MRG waves that have eastward group velocity. Once again, many of the models have wind anomalies that exceed the magnitude of the wind anomaly in ERAI. The longitude-latitude composite maps for horizontal winds and temperature anomalies in Figure 10 confirm that these are indeed MRG waves and that there is also substantial variability among the models.

5 | RESOLVED WAVE FORCING IN THE QBOI MODELS

The zonal force due to wave-mean flow interactions is typically described using the Transformed Eulerian Mean (TEM) formalism (Andrews and McIntyre, 1976). The zonal-mean zonal momentum equation in pressure coordinates is:

$$\frac{\partial \overline{u}}{\partial t} - \overline{v}^* \left[f - \frac{\partial (\overline{u} \cos\phi)}{a \cos\phi \, \partial\phi} \right] + \overline{w}^* \frac{\partial \overline{u}}{\partial p} = \frac{\nabla \cdot \mathbf{F}}{a \cos\phi} + \overline{X} \tag{3}$$

where the wave forcing on the mean flow (zonal-mean acceleration) is proportional to the divergence of the Eliassen-Palm flux (EP flux) vector (**F**):

$$\frac{1}{a \cos\phi} \nabla \cdot \mathbf{F} = \frac{1}{a \cos\phi} \left[\frac{\partial (F_\phi \cos\phi)}{a \cos\phi \, \partial\phi} + \frac{\partial F_p}{\partial p} \right] \tag{4}$$

and u, v, w are zonal, meridional, and vertical pressure velocity, f is the Coriolis parameter, a is Earth's radius, ϕ is latitude, p is pressure, and X represents any other dissipative force. Overbars denote zonal means, and $\overline{v}^*$ and $\overline{w}^*$ define the TEM or residual circulation.

To examine the QBO zonal mean momentum budget, the terms from the TEM zonal-mean zonal momentum equation (3) were computed following the method outlined for The Dynamics and Variability Model Intercomparison Project (DynVarMIP) by Gerber and Manzini (2016a,b) (see Butchart et al. (2018) for further details). Figure 11 shows the zonal-mean acceleration due to EP flux divergence (Equation 4) for all resolved waves in the QBOi models averaged between 10°S and 10°N as a function of pressure and time. This plot uses 10 years of monthly mean model output between January 1990 and December 1999. Zonal acceleration due to EP flux divergence is shown in the color contours, and the zonal-mean zonal wind is shown in the black contours. There is a large spread among the models in the magnitude of forcing from resolved waves. All but one (MIROC-AGCM-LL) of the QBOi models rely on parameterized nonorographic gravity wave drag to drive the QBO. In the models that rely on parameterized gravity wave drag, the nonorographic gravity wave forcing ranges from being roughly equal to the resolved wave forcing to being many times larger than the resolved wave forcing. For a comparison of the resolved wave forcing to the parameterized wave forcing, we refer the reader to Bushell et al. (Paper 1, characterization of present-day QBOs) in this Special Section. The zonal-mean forcing due to EP flux divergence is generally concentrated in the areas of highest vertical shear in the zonal winds, near the zero-wind line, especially for eastward forcing. Eastward forcing is also larger than westward forcing in most of the models except maybe for 60LCAM, which is also the model with largest MRG waves in Figure 5. For the other models this is consistent with previous studies (e.g. Giorgetta et al., 2002; Kawatani et al., 2010; Holt et al., 2016). Note also that this result can depend on the latitude range (if the average is performed close to the equator, the westward forcing can be substantial). For example, Garcia and Richter (2019) showed that the resolved wave forcing and paramaterized nonorographic gravity wave forcing at 25 hPa were approximately equal in CESM1(WACCM-110L) when averaged over ±2.36° latitude. This is discussed further in Section 5.1.

It is difficult to evaluate the wave forcing from models with respect to observations since we do not have global observations of wave forcing for the entire spectrum of waves in the real atmosphere. One way to estimate the total wave forcing is to evaluate the left hand side (LHS) of Equation 3 using reanalysis winds and temperatures. To do this we use ERAI since it has a QBO-like oscillation that closely matches the observed QBO and compute the total zonal force using the method described in Holt et al. (2016). Briefly, the method consists of evaluating $\partial u/\partial t$ as well as the advective terms on the LHS of Equation 3, which in turn requires estimating $\overline{v}^*$ and $\overline{w}^*$. This sum is assumed to equal the total wave forcing on the RHS of Equation 3. Figure 12 shows the total zonal-mean zonal force estimated from the LHS of Equation 3 using ERAI data compared to the resolved wave forcing in the QBOi models averaged over westward (left) and eastward (right) shear zones and 10°S to 10°N as a function of pressure. Westward shear zones are simply defined to be all instances when $\partial\overline{u}/\partial z < 0$ and eastward shear zones are all instances when $\partial\overline{u}/\partial z > 0$. Note that the magnitude of the forcing in Figure 12 is not as large as those in Figure 11 as a result of averaging over the entire area where $\partial\overline{u}/\partial z < 0$ or $\partial\overline{u}/\partial z > 0$. As seen in Figure 11, the largest forcing concentrates in the regions of strongest shear.

To obtain a realistic QBO-like oscillation in models, the sum of the resolved and parameterized wave forcing should be close to the ERAI total zonal-mean zonal force. This figure illustrates why all but one of the models require parameterized gravity wave drag to obtain a QBO-like oscillation. The resolved wave forcing is typically two or more times smaller than the estimated total zonal-mean zonal forcing required to obtain a realistic QBO-like oscillation. Furthermore, the forcing in eastward shear zones is negative for some of the QBOi models, so that the parameterized gravity waves must overcompensate to obtain the modeled QBO-like oscillations. Some of the features of this plot might be different if different latitude bands were chosen. For example, some of the large negative values below 50 hPa in the right panel of the plot are likely due to large forcing from tropical Rossby waves, which would not be present very close to the equator.

Figure 13 shows the latitude-pressure distribution of the resolved wave forcing during descending eastward and westward phases of the QBO in the QBOi models. The descending eastward phase is shown on the left side of each

model panel, and the descending westward phase is on the right side of each model panel. The descending eastward or westward phase is defined as the time when the eastward or westward winds reach 30 hPa. The composites are constructed from monthly-mean output by averaging over the months that met the criteria for descending eastward or westward phase. Overall there is better inter-model agreement during the descending eastward phase of the QBO. The models generally show a broad arc of eastward wave forcing around the level of maximum vertical shear in the zonal-mean zonal winds that increases in altitude with latitude. The magnitude of eastward forcing varies greatly as was seen in Figure 11.

During the descending westward phase most of the models show an area of westward wave forcing that is more confined in latitude to regions near the equator. CESM1(WACCM-110L) in particular but also ECHAM5sh and MIROC-ESM have strong westward forcing in a narrow latitude band about the equator. In many of the models this region of westward wave forcing is flanked by eastward wave forcing. These structural differences are overlooked when considering only averages about the equator and may explain why many previous studies that average over a wider latitude band suggest that eastward equatorial wave forcing is larger than westward equatorial forcing (Garcia and Richter, 2019).

5.1 | Spectral decomposition of the resolved wave forcing

In this section we investigate the spectral distribution of the resolved wave forcing in the QBOi models. The components of the EP flux vector can be computed as a function of zonal wavenumber, k, and frequency, ω (Horinouchi et al., 2003):

$$F_\phi(k,\omega) = a\cos\phi\left\{\frac{\Re[V\widetilde{\Theta}]}{\partial\bar{\theta}/\partial p}\frac{\partial\bar{u}}{\partial p} - \Re[U\widetilde{V}]\right\}$$

$$F_p(k,\omega) = a\cos\phi\left\{\frac{\Re[V\widetilde{\Theta}]}{\partial\bar{\theta}/\partial p}\left[f - \frac{\partial(\bar{u}\cos\phi)}{a\cos\phi\,\partial\phi}\right] - \Re[U\widetilde{W}]\right\} \quad (5)$$

where $\Re$ denotes the real part and the tilde denotes the complex conjugate. U, V, W, and Θ are functions of k and ω such that $U(k,\omega)$, $V(k,\omega)$, $W(k,\omega)$, and $\Theta(k,\omega)$ are the two-dimensional Fourier transforms of $u(\lambda,t)$, $v(\lambda,t)$, $w(\lambda,t)$, and $\theta(\lambda,t)$, where λ is longitude and t is time.

Figure 14 shows the wavenumber-frequency spectrum of the vertical component of the EP flux vector, F_p, averaged over 10 years (except UMGA7 and UMGA7gws, which only had 6 years of 6-hourly files available) between 10°S and 10°N and over the pressure range ~85–70 hPa. Phase speed lines are also shown in the black contours. To compute the EP flux spectra for the QBOi models, we used 6-hourly winds and temperature. We computed the fast Fourier transform using a 72-day window and 12-day overlap, resulting in 60 windows over the 10-year period. After the fast Fourier transform was computed for each time window, the windows were averaged in time and latitude from 10°S and 10°N and over the pressure range ~85–70 hPa. We note that some positive flux appears at negative zonal wavenumbers and some negative flux appears at positive zonal wavenumbers mostly because the phase speeds are relative to the ground and not the background wind. There is a large inter-model spread in the magnitude of the EP fluxes and also in the preferred phase speeds. This is consistent with Horinouchi et al. (2003), who also found a very large inter-model spread in both the magnitude and preferred phase speeds of EP fluxes at 65 hPa. Additionally, some models tend to have a narrow range of preferred phase speeds, while others have quite a broad range.

Observationally derived EP flux estimates show a double lobe structure in phase speed, meaning two lobes for

eastward propagating waves and two lobes for westward propagating waves, with preferred phase speeds of ±15 and ±45 m s^{-1} (Ricciardulli and Garcia, 2000). The double lobe structure becomes more pronounced at high frequencies. High-resolution models also show a double lobe structure in phase speed (Holt et al., 2016). None of the models have much of a double lobe structure for either eastward or westward propagating waves and instead tend to have one preferred phase speed ranging anywhere from 5 to 50 m s^{-1}. There is some evidence of a double lobe structure emerging in the models with more power at higher frequencies, especially MIROC-ESM, but not at the observed phase speeds. In general, the models that have higher preferred phase speeds tend to have more power concentrated at longer wavelengths and lower frequencies, whereas the models that have the lowest preferred phase speeds have power that extends more to the smaller scales. It is interesting to note that three models with very similar EP flux spectra with more power at smaller scales (AGCM3-CMAM, EMAC, and MIROC-ESM) have very different precipitation spectra and very different levels of CCKW organization. AGCM3-CMAM has no power at the smaller scales in Figure 1, weak organization along preferred phase speed lines, and no organization into CCKW modes in Figure 2. EMAC has more power at the smaller scales in Figure 1, some organization along preferred phase speed lines, and weak organization into CCKW modes in Figure 2. MIROC-ESM has some power at the smaller scales in Figure 1, strong organization along preferred phase speed lines, and strong organization into CCKW modes in Figure 2.

Figure 15 shows the wavenumber-frequency distribution of the resolved wave forcing near 25 hPa for different shear zones in the QBOi models. The EP flux divergence was computed with Equation 4, where $F_\phi(k,\omega)$ and $F_p(k,\omega)$ were computed with Equation 5 with 6-hourly data. The left side of each model panel shows the resolved wave forcing in strong westward shear and the right side of each model panel shows the resolved wave forcing in strong eastward shear. Most of the models show a strong westward forcing at phase speeds between -20 and -5 m s^{-1} but with a wide range of zonal wavenumbers (typically between -10 and -1) and frequencies (typically less than 0.3 cpd). 60LCAM5, CESM1(WACCM-110L), ECHAM5sh, LMDz6, MIROC-AGCM-LL, MIROC-ESM, and UMGA7 show peaks at wavenumbers corresponding to the peaks in Figure 5 (typically near k=-5). These models also show convective organization into MRG wave modes at the same wavenumbers in Figure 3. Some models also show eastward forcing at low wavenumbers and frequencies during strong westward shear. There is better agreement among the model forcing for strong eastward shear. Most of the models show forcing with preferred phase speeds near 20 m s^{-1} and between wavenumbers 1 and 10 and frequencies less than 0.45 cpd. Models with strong CCKW organization do tend to show strong forcing along the 20 m s^{-1} phase speed line (60LCAM5, CESM1(WACCM-110L), ECHAM5sh, MIROC-AGCM-LL). Just as some models show eastward forcing during strong westward shear, some of the models show westward forcing during strong eastward shear, particularly between westward (negative) wavenumbers 5 and 10. For example, CESM1(WACCM-110L) shows westward propagating waves centered around k=8. This has been associated with RG waves excited by barotropic instability on the upper side of the eastward jet and has been discussed in detail by Garcia and Richter (2019).

5.2 | Kelvin waves and QBO forcing

Next we investigate the contribution of large-scale eastward propagating equatorial waves to the resolved wave forcing. Figure 16 shows the zonal acceleration due to EP flux divergence from eastward propagating waves with wavenumbers $1 \leq k \leq 10$ and frequencies less than 0.5 cpd as a function of pressure and time for 3 years. Note that the chosen three years vary between models, depending on the periods when 6-hourly output was available. The 6-hourly EP flux divergence spectra for each month are integrated over the above subset of the wavenumber-frequency domain and then averaged from 10°S to 10°N. As with the total resolved wave forcing in Figure 11 there is a large spread among the models in the magnitude of the large-scale eastward wave forcing, although all models do show at least some

large-scale eastward wave activity in the eastward shear zones, however small. Likewise as in Figure 11, the forcing is generally concentrated around regions of high vertical shear in the zonal-mean zonal wind near the zero-wind line. The magnitudes are also similar to what is seen in Figure 11, which implies that most of the eastward forcing is due to eastward-propagating waves of $k = 1 - 10$.

There are some observational estimates of Kelvin wave forcing to compare to. For example, Alexander and Ortland (2010) estimated with HIRDLS data that peak values in the monthly mean wave forcing due to Kelvin waves is around 0.5 m s^{-1} day^{-1} between 20-10 hPa and around 0.2 m s^{-1} day^{-1} between 50-20 hPa. A few of the models do show values that are consistent with the HIRDLS estimates, but many of the models are too low.

There does seem to be a relationship between the strength of the CCKWs and the magnitude of the large-scale eastward wave forcing in Figure 16. This relationship has also been suggested by previous model intercomparison studies (e.g., Horinouchi et al., 2003). In general the models that have stronger CCKW signals in precipitation in Figure 2 have greater eastward wave forcing in the eastward shear zones in Figure 16. However, there are exceptions to this relationship. For example, 60LCAM5 has the strongest organization of precipitation variability into Kelvin wave modes, but the eastward wave forcing is relatively weak. As we pointed out at in Section 4, 60LCAM has a strong eastward bias in the lower stratosphere. Interestingly, 60LCAM5 also has the largest difference between tropospheric and stratospheric vertical resolution (less than 0.5 km between 10–15 km and nearly 0.8 km between 20–25 km; see Figure 5 in Butchart et al. (2018)). Other exceptions to this relationship appear to be LMDz6 and UMGA7. For example, LMDz6 has stronger CCKWs than MIROC-ESM in Figure 2, but MIROC-ESM has much stronger Kelvin wave forcing in Figure 16. Likewise, UMGA7 has stronger CCKWs than EMAC in Figure 2, but EMAC has stronger Kelvin wave forcing in Figure 16. LMDz6 and UMGA7 have some of the coarsest vertical resolutions the QBO region (LMDz6~1.1 km, UMGA7~0.82 km) compared to other QBOi models. Finally, there also seems to be a general dependence of the magnitude of eastward forcing on the dynamical core. Models that have an Eulerian or Eulerian/spectral transform dynamical core (AGCM3-CMAM, ECHAM5sh, EMAC, LMDz6, MIROC-AGCM-LL, MIROC-ESM) tend to have greater eastward forcing in the eastward shear zones than models with a semi-Lagrangian/semi-implicit dynamical core (HadGEM2-A, HadGEM2-AC, MRI-ESM2, UMGA7, and UMGA7gws). There is only one model with a finite volume dynamical core (CESM1(WACCM-110L)) and one model with a spectral element dynamical core (60LCAM5), so it is not possible to draw conclusions about those dynamical cores. Next we will explore these model parameters more quantitatively.

Ideally to compare the wave forcing from different models, we would have identical wind profiles to control for the differences in wave forcing due to differences in wind. Since the models are free-running, this is not the case. Instead we compare the zonal forcing due to large-scale eastward propagating waves for similar zonal wind profiles. For wave dissipation the location of the zero-wind line is the most important feature when comparing wind profiles. The left plot in Figure 17 shows zonal-mean zonal wind profiles for the QBOi models when the zero-wind line is between about 17-13 hPa during a descending eastward shear zone. The right plot in Figure 17 shows the profile of zonal forcing due to large-scale eastward propagating waves for the winds in the left panel. As shown in the figure, the wave forcing varies greatly even in very similar wind profiles. It is extremely challenging to tease apart all of the variables in each model that might contribute to the varying magnitudes of resolved wave forcing. However, one relatively straightforward variable to investigate is model resolution.

Figure 18 shows how the wave forcing due to large-scale eastward propagating waves relates to model vertical and horizontal resolution (different symbols denote different dynamical core types as described in the figure caption). The wave forcing is calculated by averaging the profiles on the right side of Figure 17 between 26 and 10 hPa. Even though the QBOi models have very different formulations, there is a clear relationship between the wave forcing and model vertical resolution in the lower stratosphere (between 20–25 km). The Pearson correlation coefficient between wave forcing and vertical grid spacing is -0.6, while the Pearson correlation coefficient between wave forcing and horizontal

grid spacing is 0.3. Since we expect that the wave forcing should also vary inversely with horizontal grid spacing (e.g., Holt et al., 2016), the fact that there is instead a small positive correlation is perhaps a measure of the confounding factors due to the complexity of the models. This suggests that the relationship between wave forcing and model vertical resolution would be even stronger if the confounding factors were controlled for.

The importance of sufficient model vertical resolution for representing equatorial waves has been known for some time. Boville and Randel (1992) showed that vertical resolution of less than 1 km was required to accurately represent equatorial waves. Richter et al. (2014) obtained a realistic model QBO-like oscillation in CAM with a vertical resolution of 500 m. They found that the model generated the realistic QBO-like oscillation even when the horizontal resolution was 200 km as long as the vertical resolution was 500 m. Anstey et al. (2016) showed that vertical resolution of less than 1 km in the lower stratosphere was necessary for CMAM to exhibit a realistic QBO-like oscillation. Holt et al. (2016) showed that a doubling of the vertical resolution resulted in a doubling of the wave forcing in strong westward shear, whereas a factor-of-16 increase in horizontal resolution only quadrupled the wave forcing. Giorgetta et al. (2006) also found that the simulated QBO-like oscillation in a GCM was much more sensitive to changes in vertical resolution than horizontal resolution.

The right panel of Figure 18 shows the relationship between CCKWs in Figure 2 and wave forcing due to large-scale eastward propagating waves in the QBO region. The strength of the CCKWs was computed as the average of the ratio in 2 for wavenumbers between 1 and 10 and frequencies between 0.1 and 0.3 cpd. The Pearson correlation coefficient between wave forcing and CCKW strength is 0.4. The exceptions to this apparent relationship discussed above (60LCAM5, LMDz6, and UMGA7) show up as clear outliers in the plot as well. In fact, if they are removed the Pearson correlation coefficient goes up to 0.9, indicating a very strong relationship between the magnitude of wave forcing in the QBO region and the strength of the CCKWs in the troposphere. Interestingly, there is no relationship between the strength of CCKWs and vertical grid spacing in the troposphere (not shown). These results together suggest that CCKWs do have an influence over the wave forcing in the QBO region, but the model needs to have sufficient vertical resolution in the QBO region for this relationship to become apparent.

Figure 18 also shows that the wave forcing in models with a semi-Lagrangian/semi-implicit advection scheme does tend to be lower than in models with an Eulerian/spectral transform advection scheme. CESM1(WACCM-110L) is the only model participating in the QBOi with a finite volume advection scheme. It is interesting that CESM1(WACCM-110L) has the strongest wave forcing considering that Yao and Jablonowski (2015) found the finite volume dynamical core did not sustain a QBO-like oscillation and had weaker wave activity and forcing compared to Eulerian/spectral transform, spectral element, and semi-Lagrangian versions of the same idealized model. It is worth noting that the idealized models used by Yao and Jablonowski (2015) all had 2° horizontal resolution and 1.25 km vertical resolution in the stratosphere, whereas CESM1(WACCM-110L) used $\approx 1°$ horizontal resolution and 500 m vertical resolution in the stratosphere up to about 10 hPa. Perhaps the increase in horizontal and vertical resolution leads to improvement in the representation of dissipative processes. In any case, it is not clear whether the increased vertical resolution is needed to represent the waves or to represent the wave-mean flow interactions accurately (or both).

6 | SUMMARY AND CONCLUSIONS

In this paper we evaluated equatorial waves and their role in driving the QBO-like oscillations in models participating in the QBOi. The QBOi models vary widely in their ability to simulate the overall variability in precipitation and also in their ability to simulate convectively coupled waves. This result is consistent with previous model comparisons (e.g., Lin et al., 2006; Straub et al., 2010; Lott et al., 2014) and suggests that simulating precipitation variability and convectively

coupled modes is still a major issue. 8 of the 13 QBOi models investigated here reasonably simulate convectively coupled Kelvin waves, and only a few of the QBOi models investigated here reasonably simulate convectively coupled mixed Rossby-gravity waves. In this sense, the ability of the QBOi models to simulate convectively coupled waves is only slightly improved compared to CMIP5 and CMIP3 models. In general, there does not seem to be a relationship between vertical resolution in the upper troposphere and the strength of the simulated convectively coupled waves.

Regardless of the major differences among the QBOi models with respect to precipitation variability and convectively coupled waves, most of the QBOi models have robust Kelvin and MRG waves in the lower stratosphere and represent them better than most of the CMIP5 models. Interestingly, while there does seem to be some correlation between the strength of CCKWs and Kelvin wave forcing in the QBO region, the models with the strongest CCKWs are not necessarily the ones with the strongest Kelvin wave forcing in the eastward QBO shear zones. The reasons discussed were insufficient vertical resolution and a strong eastward bias in one of the models. This could also suggest that convectively coupled waves may not have as strong of an influence on stratospheric equatorial waves as previously thought. This is supported by recent research which suggests that filtering by the mean winds plays a large role in determining the momentum fluxes near the tropopause (Warner et al., 2005; Alexander et al., 2017). Another explanation could be that convectively coupled waves tend to be rather slow and may be important only in the lower stratosphere, whereas at higher levels, faster waves that are forced by convection, but not coupled to it, predominate.

Even though most of the QBOi models have robust Kelvin and MRG waves in the lower stratosphere, the wave forcing in the QBO region is too low compared to the forcing required to drive the observed QBO. In all but one (MIROC-AGCM) of the QBOi models, parameterized gravity waves provide at least half of the forcing for the QBO-like oscillations (see Bushell et al. (2019), part of this special section). It is important to note that this is based on 10°S–10°N averages. The lack of resolved wave forcing is common in climate simulations and is typically due to various factors such as vertical resolution and implicit and explicit numerical dissipation. In the QBOi models, despite the varying setups, vertical resolution emerged as a clear factor controlling the degree of wave forcing in the eastward QBO shear zones.

7 | ACKNOWLEDGEMENTS

We acknowledge the scientific guidance of the WCRP for helping motivate this work, coordinated under the framework of the Stratosphere-troposphere Processes and their Role in Climate (SPARC) QBO initiative (QBOi) led by JA, NB, KH and SO. The QBOi data archive was kindly hosted by the Centre for Environmental Data Analysis (CEDA). LH was supported by the NASA Global Modeling and Assimilation Office (GMAO) Grant #NNX14O76G, the NASA Atmospheric Composition Modeling and Analysis Program (ACMAP) Grant #80NSSC18K0069, and the NASA Modeling, Analysis and Prediction (MAP) program Grant #80NSSC17K0169. This material is based upon work supported by the National Center for Atmospheric Research, which is a major facility sponsored by the National Science Foundation under Cooperative Agreement No. 1852977. The CESM project is supported primarily by the National Science Foundation. Portions of this study were supported by the Regional and Global Model Analysis (RGMA) component of the Earth and Environmental System Modeling Program of the U.S. Department of Energy's Office of Biological & Environmental Research (BER) via National Science Foundation IA 1947282. 60LCAM5 and CESM1(WACCM-110L) simulations were carried out on the Yellowstone high-performance computing platform. FL and SO were supported by the JPI-Climate/Belmont Forum project GOTHAM (ANR-15-JCLI-0004-01, NERC NE/P006779/1). YMC was supported as an National Research Council Fellow through the Physical Sciences Division of ESRL/NOAAFor the EMAC simulations, PB, TK, and SV acknowledge support by the state of Baden-Württemberg through bwHPC. YK was supported by Japan Society for Promotion of Science (JPSP) KAKENHI Grant Numbers JP15KK0178, JP17K18816 and JP18H01286. YK and KH were supported

by the Japan Agency for Marine-Earth Science and Technology (JAMSTEC) through its sponsorship of research at the International Pacific Research Center. SW and YK were partly supported by a Japan Science and Technology Agency (JST) as part of the Belmont Forum, and by the "Integrated Research Program for Advancing Climate Models (TOUGOU program)" from the Ministry of Education, Culture, Sports, Science and Technology (MEXT), Japan. The Earth Simulator was used for MIROC-ESM and MIOC-AGCM-LL simulations. CC and FS have been supported by the Copernicus Climate Change Service, funded by the EU and implemented by ECMWF. NB and AAS were supported by the Met Office Hadley Centre Climate Programme funded by BEIS and Defra.

REFERENCES

Adachi, Y., Yukimoto, S., Deushi, M., Obata, A., Nakano, H., Tanaka, T. Y., Hosaka, M., Sakami, T., Yoshimura, H., Hirabara, M., Shindo, E., Tsujino, H., Mizuta, R., Yabu, S., Koshiro, T., Ose, T. and Kitoh, A. (2013) Basic performance of a new earth system model of the Meteorological Research Institute (MRI-ESM1). *Pap. Meteorol. Geophys.*, **64**, 1–19.

Alexander, M. J. and Ortland, D. (2010) Equatorial waves in High Resolution Dynamics Limb Sounder (HIRDLS) data. *J. Atmos. Sci.*, **115**.

Alexander, M. J., Ortland, D. A., Grimsdell, A. W. and Kim, J.-E. (2017) Sensitivity of gravity wave fluxes to interannual variations in tropical convection and zonal wind. *J. Atmos. Sci.*, **74**, 2701–2716.

Andrews, D. G. and McIntyre, M. E. (1976) Planetary waves in horizontal and vertical shear: The generalized Eliassen-Palm relation and the mean zonal acceleration. *J. Atmos. Sci.*, **33**, 2031–2048.

Anstey, J. A., Scinocca, J. F. and Keller, M. (2016) Simulating the QBO in at Atmospheric General Circulation Model: Sensitivity to Resolved and Parameterized Forcing. *J. Atmos. Sci.*, **73**, 1649–1665.

Baldwin, M. P., Gray, L. J., Dunkerton, T. J., Hamilton, K., Haynes, P. H., Randel, W. J., Holton, J. R., Alexander, M. J., Hirota, I., Horinouchi, T., Jones, D. B. A. J., Kinnersley, J. S., Marquardt, C., Sato, K. and Takahashi, M. (2001) The quasi-biennial oscillation. *Rev. Geophys.*, **39**, 179–229.

Boville, B. A. and Randel, W. J. (1992) Equatorial waves in a stratospheric GCM: Effects of vertical resolution. *J. Atmos. Sci.*, **49**, 785–801.

Bushell, A. C., Anstey, J. A., Butchart, N., Kawatani, Y., Osprey, S. M., Richter, J. H., Serva, F., Braesicke, P., Cagnazzo, C., Chen, C.-C., Chun, H.-Y., Garcia, R. R., Gray, L. J., Hamilton, K., Kerzenmacher, T., Kim, Y.-H., Lott, F., McLandress, C., Naoe, H., Scinocca, J., Smith, A. K., Stockdale, T. N., Versick, S., Watanabe, S., Yoshida, K. and Yukimoto, S. (2019) Evaluation of the quasi-biennial oscillation in global climate models for the SPARC QBO-initiative. *Quart. J. Roy. Meteor. Soc.*, **In prep**.

Bushell, A. C., Butchart, N., Derbyshire, S., Jackson, D., Shutts, G. J., Vosper, S. B. and Webster, S. (2015) Parameterized gravity wave momentum fluxes from sources related to convection and large-scale precipitation processes in a global atmosphere model. *J. Atmos. Sci.*, **72**, 4349–4371.

Butchart, N., Anstey, J. A., Hamilton, K., Osprey, S., McLandress, C., Bushell, A. C., Kawatani, Y., Kim, Y.-H., Lott, F., Scinocca, J., Stockdale, T. N., Andrews, M., Bellprat, O., Braesicke, P., Cagnazzo, C., Chen, C.-C., Chun, H.-Y., Dobrynin, M., Garcia, R. R., Garcia-Serrano, J., Gray, L. J., Holt, L., Kerzenmacher, T., Naoe, H., Pohlmann, H., Richter, J. H., Scaife, A. A., Schenzinger, V., Serva, F., Versick, S., Watanabe, S., Yoshida, K. and Yukimoto, S. (2018) Overview of experiment design and comparison of models participating in phase 1 of the SPARC Quasi-Biennial Oscillation initiative (QBOi). *Geosci. Model Dev.*, **11**, 1009–1032.

Cho, H.-K., Bowman, K. P. and North, G. R. (2004) Equatorial waves including the Madden-Julian Oscillation in TRMM rainfall and OLR data. *J. Climate*, **17**, 4387–4406.

Dee, D. P., Uppala, S. M., Simmons, A. J., Berrisford, P., Poli, P., Kobayashi, S., Andrae, U., Balmaseda, M. A., Balsamo, G., Bauer, P., Bechtold, P., Beljaars, A. C. M., van de Berg, L., Bidlot, J., Bormann, N., Delsol, C., Dragani, R., Fuentes, M., Geer, A. J., Haimberger, L., Healy, S. B., Hersbach, H., Hólm, E. V., Isaksen, L., Kållberg, P., Köhler, M., Matricardi, M., McNally, A. P., Monge-Sanz, B. M., Morcrette, J.-J., Park, B.-K., Peubey, C., de Rosnay, P., Tavolato, C., Thépaut, J.-N. and Vitart, F. (2011) The ERA-Interim reanalysis: configuration and performance of the data assimilation system. *Quart. J. Roy. Meteor. Soc.*, **137**, 553–597.

Dunkerton, T. J. (1997) The role of gravity waves in the quasi-biennial oscillation. *J. Geophys. Res.*, **102**, 26053–26076.

Ern, M., Ploeger, F., Preusse, P., Gille, J. C., Gray, L. J., Kalisch, S., Mlynczak, M. G., III, J. M. R. and Riese, M. (2014) Interaction of gravity waves with the QBO: A satellite perspective. *J. Geophys. Res. Atmos.*, **119**, 2329–2355.

Ern, M. and Preusse, P. (2009) Quantification of the contribution of equatorial Kelvin waves to the QBO wind reversal in the stratosphere. *Geophys. Res. Lett.*, **36**.

Flannaghan, T. J. and Fueglistaler, S. (2013) The importance of the tropical tropopause layer for equatorial Kelvin wave propagation. *J. Geophys. Res. Atmos.*, **118**, 5160–5175.

Garcia, R. and Richter, J. (2019) On the momentum budget of the quasi-biennial oscillation in the Whole Atmosphere Community Climate Model. *J. Atmos. Sci.*, **0**, 0.

Garcia, R. R. and Salby, M. L. (1987) Transient response to localized episodic heating in the tropics. Part II: Far-field behavior. *J. Atmos. Sci.*, **44**, 499–530.

Garfinkel, C. I., Fouxon, I., Shamir, O. and Paldor, N. (2017) Classification of eastward propagating waves on the spherical Earth. *Quart. J. Roy. Meteor. Soc.*, **143**, 1554–1564.

Geller, M. A., Alexander, M. J., Love, P. T., Bacmeister, J., Ern, M., Hertzog, A., Manzini, E., Preusse, P., Sato, K., Scaife, A. A. and Zhou, T. (2013) A comparison between gravity wave momentum fluxes in observations and climate models. *J. Climate*, **26**, 6383–6405.

Gerber, E. P. and Manzini, E. (2016a) Corrigendum to "The Dynamics and Variability Model Intercomparison Project (DynVarMIP) for CMIP6: assessing the stratosphere–troposphere system" published in Geosci. Model Dev., 9, 3413–3425, 2016. *Geosci. Model Dev.*

— (2016b) The Dynamics and Variability Model Intercomparison Project (DynVarMIP) for CMIP6: assessing the stratosphere–troposphere system. *Geosci. Model Dev.*, **9**, 3413–3425.

Giorgetta, M. A., Manzini, E. and Roeckner, E. (2002) Forcing of the quasi-biennial oscillation from a broad spectrum of atmospheric waves. *Geophys. Res. Lett.*, **29**, 1245–1248.

Giorgetta, M. A., Manzini, E., Roeckner, E., Esch, M. and Bengtsson, L. (2006) Climatology and forcing of the quasi-biennial oscillation in the MAECHAM5 model. *J. Climate*, **19**, 3882–3901.

Hamilton, K., Wilson, R. J. and Hemler, R. (1999) Middle atmosphere simulated with high vertical and horizontal resolution versions of a GCM: Improvements in the cold pole bias and generation of a QBO-like oscillation in the tropics. *J. Atmos. Sci.*, **56**, 3829–3846.

Hendon, H. H. and Wheeler, M. C. (2008) Some space-time spectral analyses of tropical convection and planetary-scale waves. *J. Atmos. Sci.*, **65**, 2936–2948.

Holt, L. A., Alexander, M. J., Coy, L., Molod, A., Putman, W. M. and Pawson, S. (2016) Tropical waves and the quasi-biennial oscillation in a 7-km global climate simulation. *J. Atmos. Sci.*, **73**, 3771–3783.

Holton, J. R. (1972) Waves in the equatorial stratosphere generated by tropospheric heat sources. *J. Atmos. Sci.*, **29**, 368–375.

Holton, J. R. and Lindzen, R. S. (1972) An updated theory for the quasi-biennial oscillation. *J. Atmos. Sci.*, **29**, 1076–1080.

Horinouchi, T., Pawson, S., Shibata, K., Langematz, U., Manzini, E., Giorgetta, M. A., Sassi, F., Wilson, R. J., Hamilton, K., de Grandprè, J. and Scaife, A. A. (2003) Tropical cumulus convection and upward-propagating waves in middle-atmosphere GCMs. *J. Atmos. Sci.*, **60**, 2765–2782.

Horinouchi, T. and Yoden, S. (1998) Wave-mean flow interaction associated with a QBO-like oscillation simulated in a simplified GCM. *J. Atmos. Sci.*, **55**, 502–526.

Jöckel, P., Kerkweg, A., Pozzer, A., Sander, R., Tost, H., Riede, H., Baumgaertner, A., Gromov, S. and Kern, B. (2010) Development cycle 2 of the Modular Earth Submodel System (MESSy2). *Geosci. Model Dev.*, **3**, 717–752.

Jöckel, P., Sander, R., Kerkweg, A., Tost, H. and Lelieveld, J. (2005) Technical note: The Modular Earth Submodel System (MESSy)–A new approach towards Earth System Modeling. *Atmos. Chem. Phys.*, **5**, 433–444.

Kawatani, Y., Hamilton, K. and Watanabe, S. (2011) The quasi-biennial oscillation in a double CO_2 climate. *J. Atmos. Sci.*, **68**, 265.

Kawatani, Y., Sato, K., Dunkerton, T. J., Watanabe, S., Miyahara, S. and Takahashi, M. (2010) The roles of equatorial trapped waves and internal intertia-gravity waves in driving the quasi-biennial oscillation. Part I: Zonal mean wave forcing. *J. Atmos. Sci.*, **67**, 963–980.

Kiladis, G. N., Dias, J. and Gehne, M. (2016) The relationship between equatorial mixed Rossby-gravity and eastward inertio-gravity waves: Part I. *J. Atmos. Sci.*, **73**, 2123–2145.

Kiladis, G. N., Wheeler, M. C., Haertel, P. T., Straub, K. H. and Roundy, P. E. (2009) Convectively coupled equatorial waves. *Rev. Geophys.*, **47**.

Kim, J.-E. and Alexander, M. J. (2013) Tropical precipitation variability and convectively coupled equatorial waves on sub-monthly time scales in reanalysis and TRMM. *J. Climate*, **26**, 3013–3030.

Kim, Y.-H. and Chun, H.-Y. (2015) Contributions of equatorial wave modes and parameterized gravity waves to the tropical QBO in HadGEM2. *J. Geophys. Res.*, **120**, 1065–1090.

Kim, Y.-H., Kiladis, G. N., Albers, J. R., Dias, J., Fujiwara, M., Anstey, J. A., Song, I.-S., Wright, C. J., Kawatani, Y., Lott, F. and Yoo, C. (2019) Comparison of equatorial wave activity in the tropical tropopause layer and stratosphere represented in reanalyses. *Atmos. Chem. Phys.*, **19**, 10027–10050.

Lawrence, B. N. (2001) A gravity-wave induced quasi-biennial oscillation in a three-dimensional mechanistic model. *Quart. J. Roy. Meteor. Soc.*, **127**, 2005–2021.

Lin, J.-L., Kiladis, G. N., Mapes, B. E., Weikmann, K. M., Sperber, K. R., Lin, W., Wheeler, M. C., Schubert, S. D., Genio, A. D., Donner, L. J., Emori, S., Gueremy, J.-F., Hourdin, F., Rasch, P. J., Roeckner, E. and Scinocca, J. F. (2006) Tropical intraseasonal variability in 14 IPCC AR4 climate models. Part I: Convective signals. *J. Climate*, **19**, 2665–2690.

Lindzen, R. S. and Holton, J. R. (1968) A theory of the quasi-biennial oscillation. *J. Atmos. Sci.*, **25**, 1095–1107.

Lott, F., Denvil, S., Butchart, N., Cagnazzo, C., Giorgetta, M. A., Hardiman, S. C., Manzini, E., Krismer, T., Duvel, J.-P., Maury, P., Scinocca, J. F., Watanabe, S. and Yukimoto, S. (2014) Kelvin and Rossby-gravity wave packets in the lower stratosphere of some high-top CMIP5 models. *J. Geophys. Res.*, **119**, 2156–2173.

Lott, F., Fairhead, L., Hourdin, F. and Levan, P. (2005) The stratospheric version of LMDz: dynamical climatologies, arctic oscillation, and impact on the surface climate. *Clim. Dynam.*, **25**, 851–868.

Lott, F., Guez, L. and Maury, P. (2012) A stochastic parameterization of non-orographic gravity waves: Formalism and impact on the equatorial stratosphere. *Geophys. Res. Lett.*, **39**.

Lott, F., Kuttippurath, J. and Vial, F. (2009) A climatology of the gravest waves in the equatorial lower and middle stratosphere: Method and comparison between the ERA-40 re-analysis and the LMDz-GCM. *J. Atmos. Sci.*, **66**, 1327–1346.

Manzini, E., Cagnazzo, C., Fogli, P. G., Bellucci, A. and Müller, W. A. (2012) Stratosphere-troposphere coupling at inter-decadal time scales: Implications for the North Atlantic Ocean. *Geophys. Res. Lett.*, **39**.

Matsuno, T. (1966) Quasi-geostrophic motions in the equatorial area. *J. Met. Soc. Japan*, **44**, 25–43.

Maury, P., Lott, F., Guez, L. and Duvel, J.-P. (2013) Tropical variability and stratospheric equatorial waves in the IPSLCM5 model. *Clim. Dyn.*, **40**, 2331–2344.

Osprey, S. M., Gray, L. J., Hardiman, S. C., Butchart, N. and Hinton, T. J. (2013) Stratospheric variability in twentieth-century CMIP5 simulations of the Met Office Climate Model: High top versus low top. *J. Climate*, **26**, 1595–1606.

Paldor, N., Fouxon, I., Shamir, O. and Garfinkel, C. I. (2018) The mixed Rossby-gravity wave on the spherical Earth. *Quart. J. Roy. Meteor. Soc.*, **144**, 1820–1830.

Ricciardulli, L. and Garcia, R. (2000) The excitation of equatorial waves by deep convection in the NCAR Community Climate Model (CCM3). *J. Atmos. Sci.*, **57**, 3461–3487.

Richter, J. H., Solomon, A. and Bacmeister, J. T. (2014) On the simulation of the quasi-biennial oscillation in the Community Atmosphere Model, version 5. *J. Geophys. Res. Atmos.*, **119**, 3045–3062.

Salby, M. L. and Garcia, R. R. (1987) Transient response to localized episodic heating in the tropics. Part I: Excitation and short-time near-field behavior. *J. Atmos. Sci.*, **44**, 458–498.

Sato, K. and Dunkerton, T. J. (1997) Estimates of momentum flux associated with equatorial Kelvin and gravity waves. *J. Geophys. Res.*, **102**, 26247–26261.

Scaife, A. A., Butchart, N., Warner, C. D., Stainforth, D., Norton, W. and Austin, J. (2000) Realistic quasi-biennial oscillations in a simulation of the global climate. *Geophys. Res. Lett.*, **27**, 3481–3484.

Scaife, A. A., Butchart, N., Warner, C. D. and Swinbank, R. (2002) Impact of a spectral gravity wave parameterization on the stratosphere in teh Met Office Unified Model. *J. Atmos. Sci.*, **59**, 1473–1489.

Schirber, S., Manzini, E. and Alexander, M. J. (2014) A convection-based gravity wave parameterization in a general circulation model: Implementation and improvements on the QBO. *J. Adv. Model. Earth Sys.*, **6**, 264–279.

Scinocca, J. F., McFarlane, N. A., Lazare, M., Li, J. and Plummer, D. (2008) Technical note: The CCCma third generation AGCM and its extension into the middle atmopshere. *Atmos. Chem. Phys.*, **8**.

Serva, F., Cagnazzo, C., Riccio, A. and Manzini, E. (2018) Impact of a stochastic nonorographic gravity wave parameterization on the stratospheric dynamics of a general circulation model. *J. Adv. Model. Earth Sys.*, **11**, 2147–2162.

Stephan, C. and Alexander, M. J. (2015) Realistic simulations of atmospheric gravity waves over the continental U.S. using precipitation radar data. *J. Adv. Model. Earth Sys.*, **7**, 823?835.

Straub, K. H., Haertel, P. T. and Kiladis, G. N. (2010) An analysis of convectively coupled Kelvin waves in 20 WCRP CMIP3 global coupled climate models. *J. Climate*, **23**, 3031–3056.

Takahashi, M. (1996) Simulation of the stratospheric quasi-biennial oscillation using a general circulation model. *Geophys. Res. Lett.*, **23**, 661–664.

Takayabu, Y. N. (1994) Large-scale cloud disturbances associated with equatorial waves. Part I: Spectral features of the cloud disturbances. *J. Meteorol. Soc. Jpn.*, **72**, 433?448.

Taylor, K., Stouffer, R. J. and Meehl, G. A. (2012) An overview of CMIP5 and the experiment design. *Bull. Amer. Meteor. Soc.*, **93**, 485–498.

The HadGEM2 Dev. Team (2011) The HadGEM2 family of Met Office Unified Model climate configurations. *Geosci. Model Dev.*, **4**, 723–757.

Walters, D., Baran, A., Boutle, I., Brooks, M., Earnshaw, P., Edwards, J., Furtado, K., Hill, P., Lock, A., Manners, J., Morcrette, C., Mulcahy, J., Sanchez, C., Smith, C., Stratton, R., Tennant, W., Tomassini, L., Weverberg, K. V., Vosper, S., Willett, M., Browse, J., Bushell, A., Dalvi, M., Essery, R., Gedney, N., Hardiman, S., Johnson, B., Johnson, C., Jones, A., Mann, G., Milton, S., Rumbold, H., Sellar, A., Ujiie, M., Whitall, M., Williams, K. and Zerroukat, M. (2017) The Met Office Unified Model Global Atmosphere 7.0/7.1 and JULES Global Land 7.0 configurations. *Geosci. Model Dev. Discuss.* In review.

Warner, C. D., Scaife, A. A. and Butchart, N. (2005) Filtering of parameterized nonorographic gravity waves in the Met Office Unified Model. *jas*, **62**, 831?1848.

Watanabe, S., Hajima, T., Sudo, K., Nagashima, T., Takemura, T., Okajima, H., Nozawa, T., Kawase, H., Abe, M., Yokohata, T., Ise, T., Sato, H., Kato, E., Takata, K., Emori, S. and Kawamiya, M. (2011) MIROC-ESM 2010: Model description and basic results of CMIP5-20c3m experiments. *Geosci. Model Dev.*, **4**, 845–872.

Watanabe, S., Kawatani, Y., Tomikawa, Y., Miyazaki, K., Takahashi, M. and Sato, K. (2008) General aspects of a T213L256 middle atmosphere general circulation model. *J. Geophys. Res.*, **113**.

Wheeler, M. and Kiladis, G. (1999) Convectively coupled equatorial waves: Analysis of clouds and temperature in the wavenumber-frequency domain. *J. Atmos. Sci.*, **56**, 374–399.

Yao, W. and Jablonowski, C. (2015) Idealized quasi-biennial oscillations in an ensemble of dry GCM dynamical cores. *J. Atmos. Sci.*, **72**, 2201–2226.

Yukimoto, S., Adachi, Y., Hosaka, M., Sakami, T., Yoshimura, H., Hirabara, M., Tanaka, T., Shindo, E., Tsujino, H., Deushi, M., Mizuta, R., Yabu, S., Obata, A., Nakano, H., Koshiro, T., Ose, T. and Kitoh, A. (2012) A new global climate model of the Meteorological Research Institute: MRI-CGCM3–Model description and basic performance. *J. Meterol. Soc. Jpn.*, **90A**, 23–64.

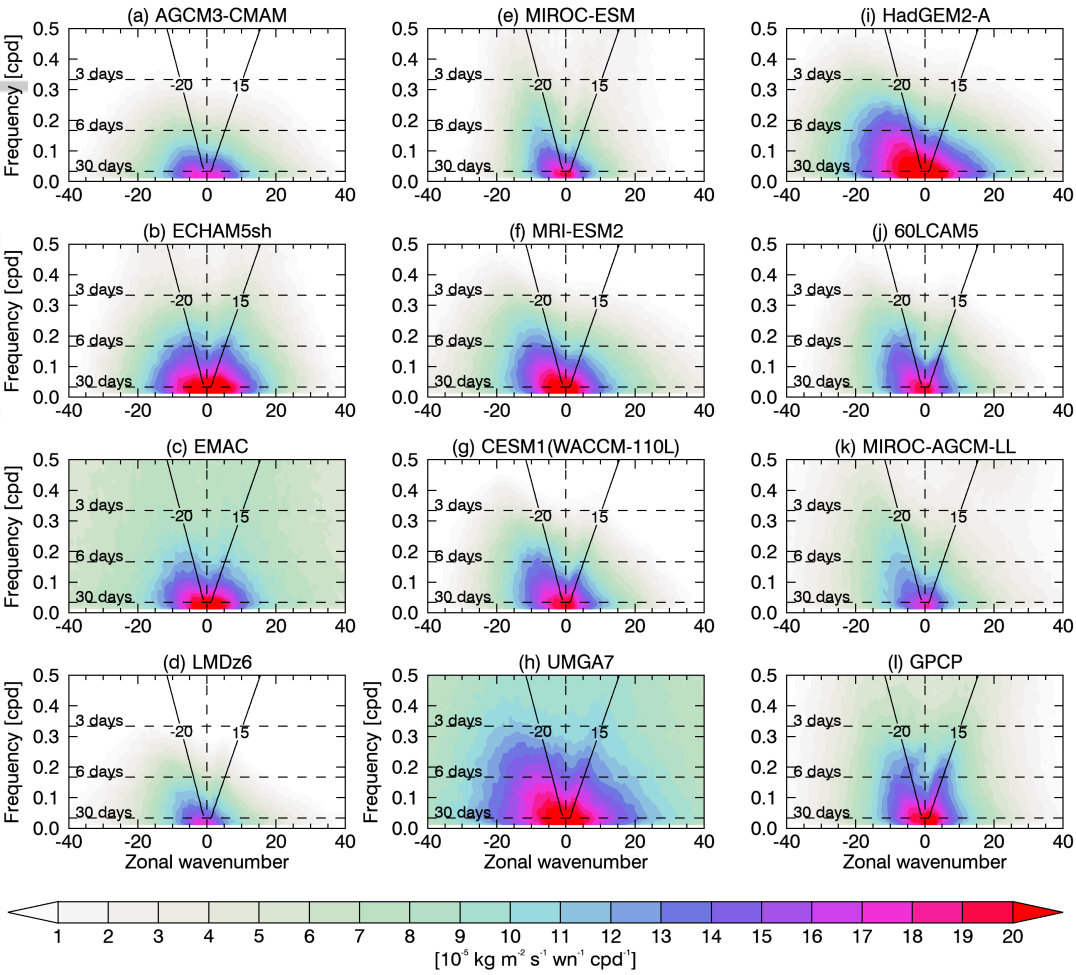

FIGURE 1 Latitudinal mean (10°S–10°N) raw precipitation power spectra as a function of wavenumber and frequency for (a)–(k) 11 QBOi models and (l) GPCP. Negative wavenumbers represent westward propagating waves. Solid lines show the zonal phase speed C_x relative to the ground for -20 m s^{-1} and 15 m s^{-1}.

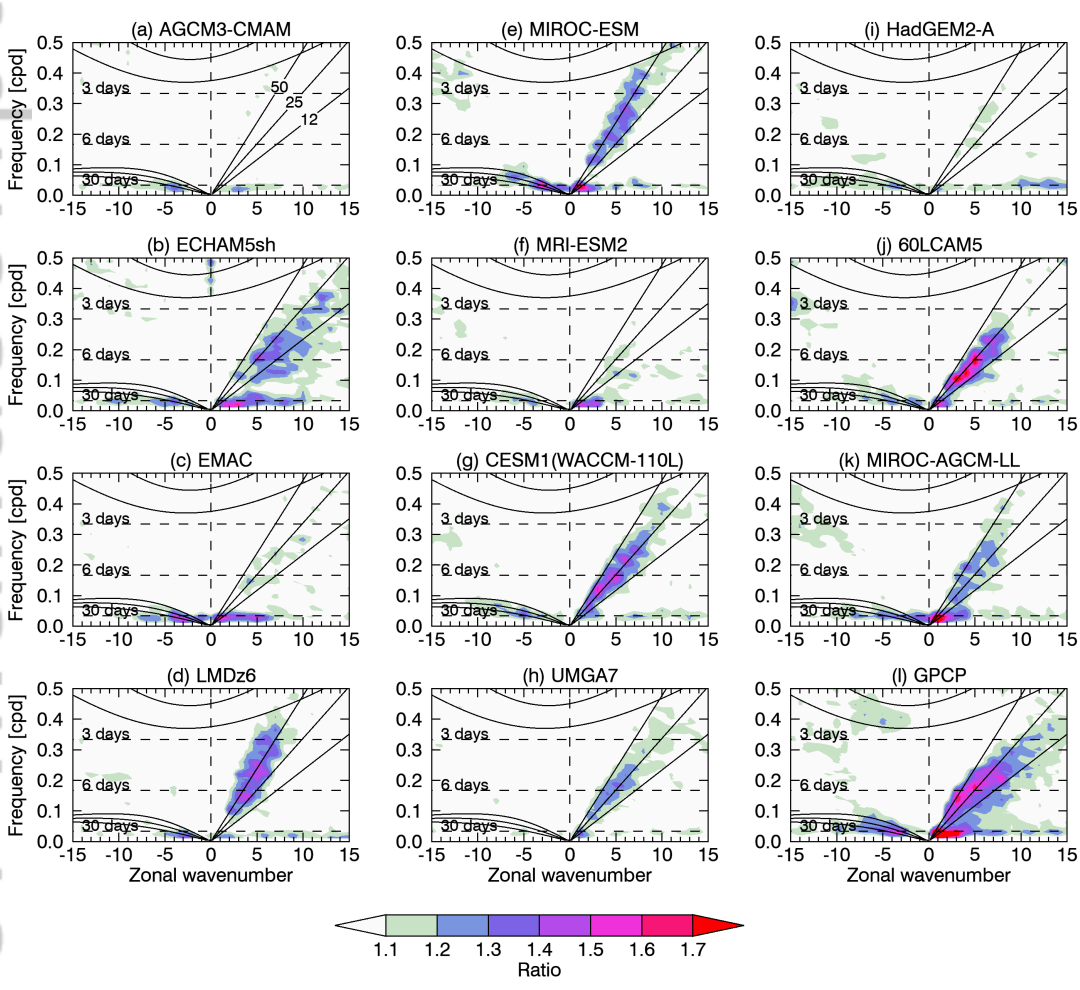

FIGURE 2 Symmetric component of the precipitation spectra as a function of wavenumber (wn) and frequency (cpd) for (a)–(k) 11 QBOi models and (l) GPCP. Negative wavenumbers represent westward propagating waves. Theoretical dispersion curves for equatorial waves with equivalent depths of 12, 25, and 50 m are also plotted, assuming a zero wind basic state (as labeled in panel (a)).

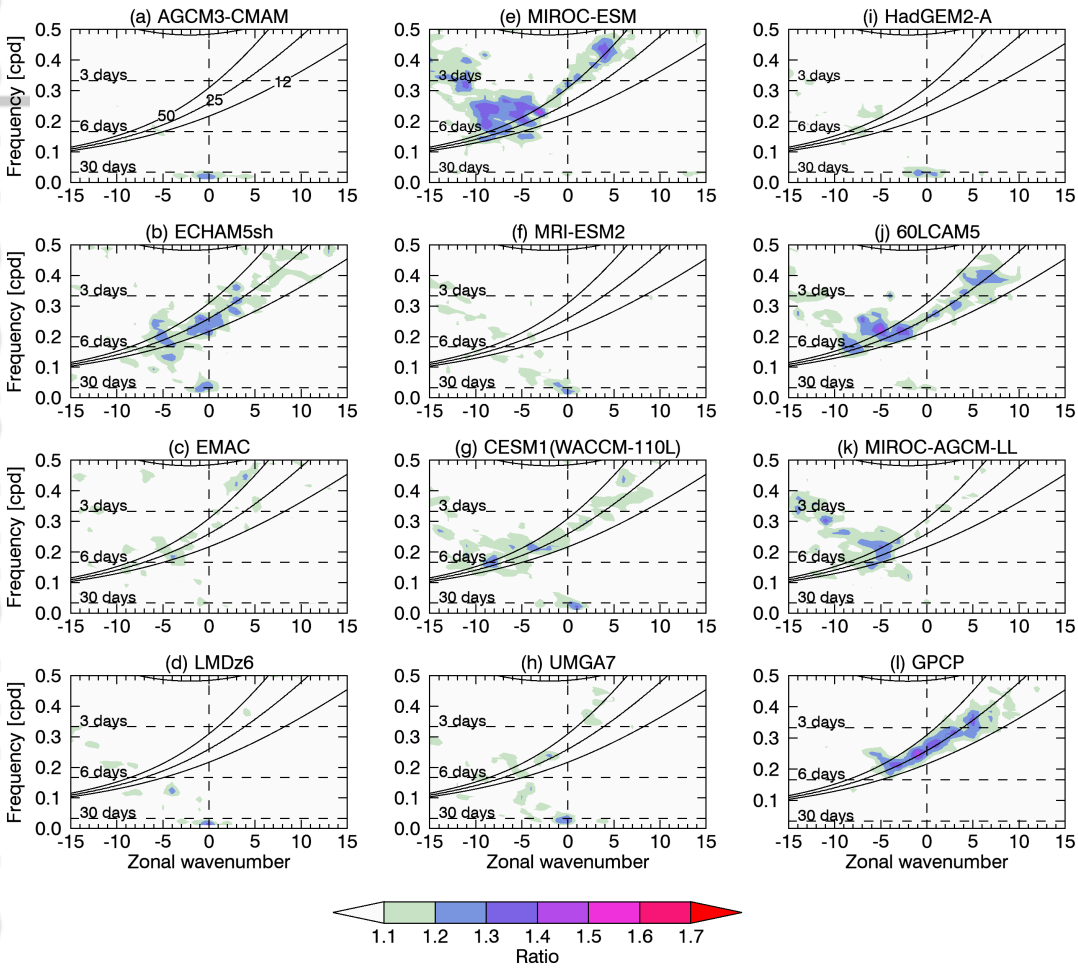

FIGURE 3 Antisymmetric component of the precipitation spectra as a function of wavenumber (wn) and frequency (cpd) for (a)–(k) 11 QBOi models and (l) GPCP. Negative wavenumbers represent westward propagating waves. Theoretical dispersion curves for equatorial waves with equivalent depths of 12, 25, and 50 m are also plotted, assuming a zero wind basic state (as labeled in panel (a)).

FIGURE 4 Spectra of the zonal wind at 50 hPa tapered in latitude by a cosine taper of 20° width centered at the equator and then averaged in latitude over the equatorial band (contour interval: 0.05 $m^2s^{-2}day^{-1}$). The thick solid lines in the eastward direction are for the Kelvin wave dispersion curves with equivalent depths of 12 m, 25 m, 50 m, and 200 m. In the westward direction the dashed lines are for the $n = 1, 3$ free planetary waves after application of a Doppler spread by an eastward wind $U = 15$ m s^{-1} to take into account advection by the midlatitude winds.

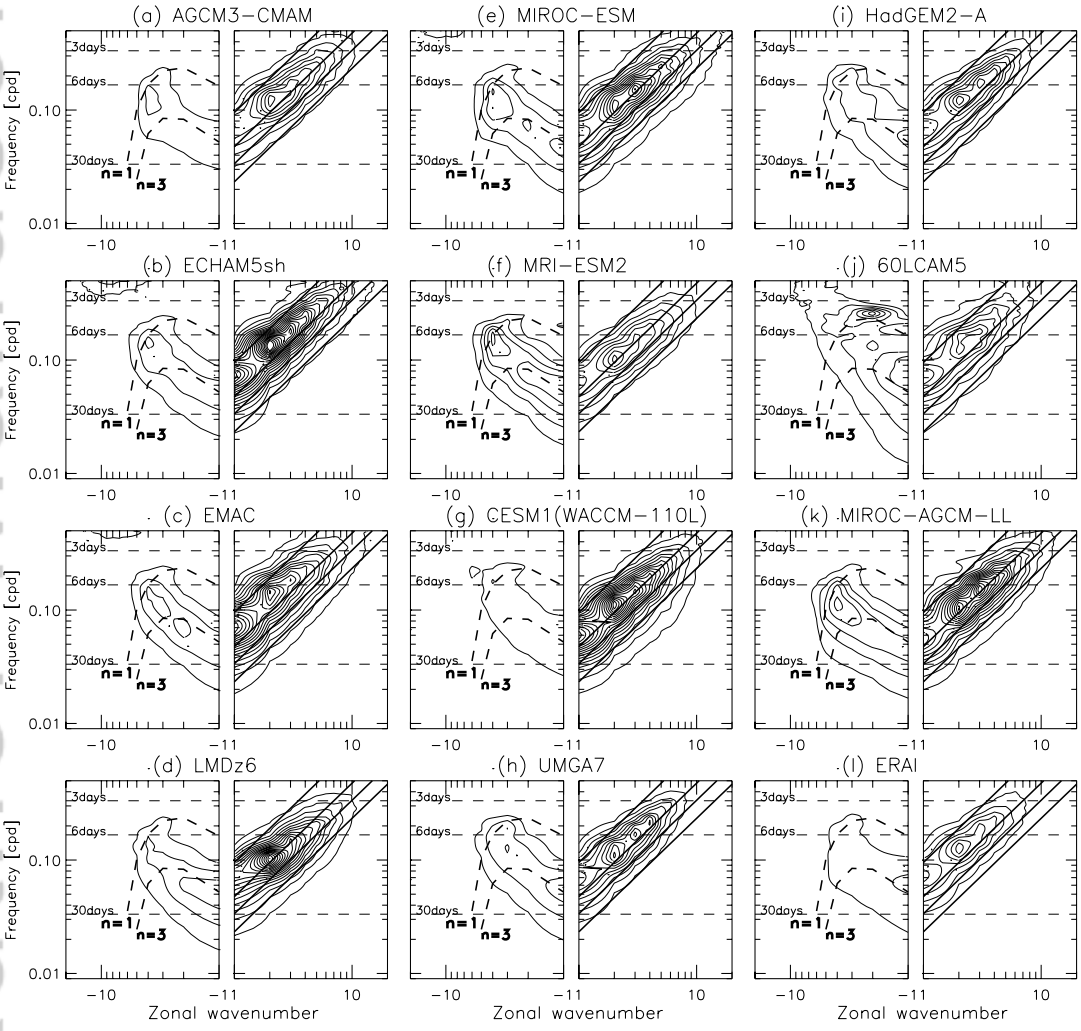

FIGURE 5 Spectra of the meridional wind at 50 hPa tapered in latitude by a cosine taper of 20° width centered at the equator and then averaged in latitude over the equatorial band (contour interval: 0.1 $m^2s^{-2}day^{-1}$). The theoretical dispersion curves for MRG waves with equivalent depths of 12 m, 25 m, and 50 m are also shown in thick solid and for 200 m in thick dashed.

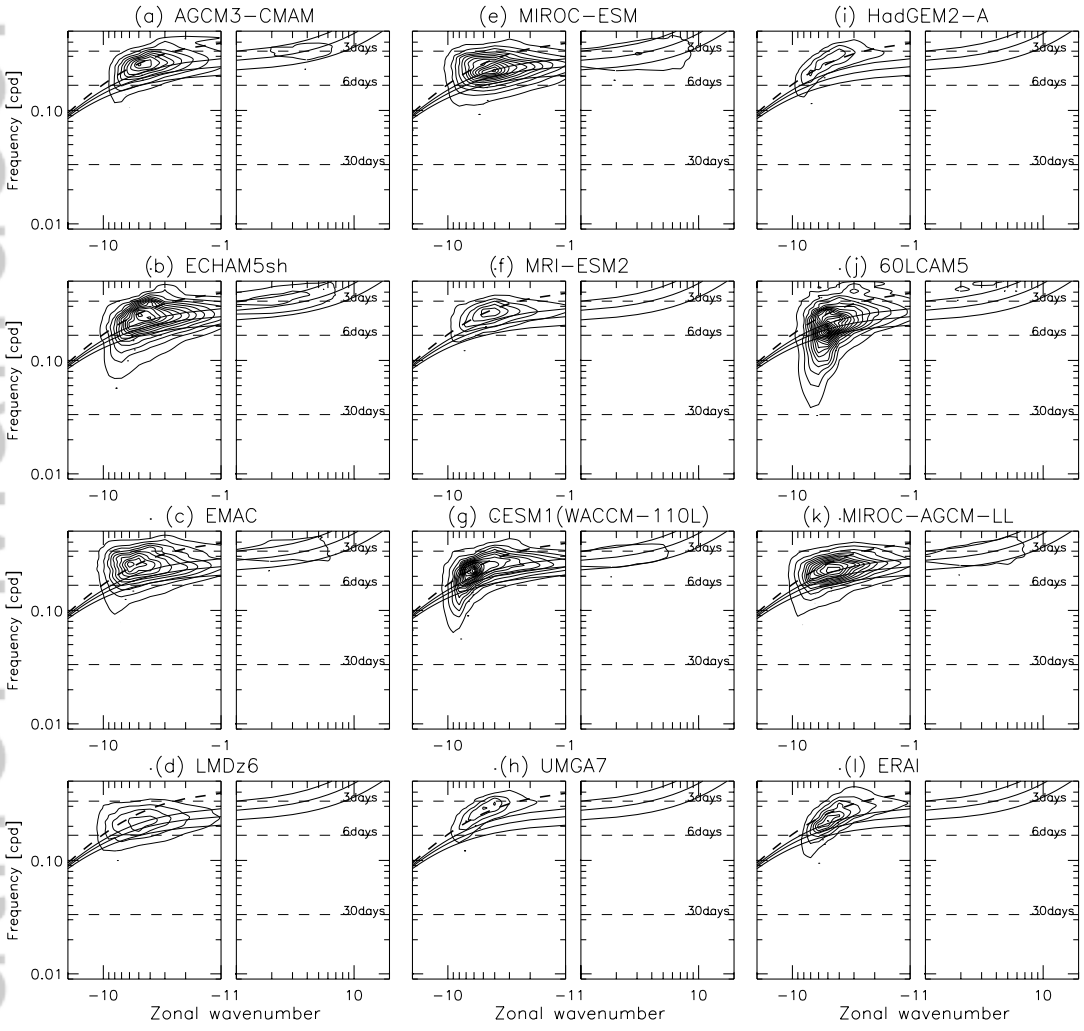

FIGURE 6 Left: Westward component of the 50 hPa spectra of the meridional wind (thin solid) and transfer function used to extract the MRG waves (thick solid, contour interval=0.2). Right: Eastward component of the 50 hPa spectra of the zonal wind and transfer function used to extract the Kelvin waves. For all models the filters are identical but the spectra shown here are from ERAI data. To estimate the spectra, the fields are tapered in latitude by a cosine taper of 20° width centered at the equator and then averaged in latitude over the equatorial band. Each year a time-longitude periodogram is then made and the spectra is estimated by averaging the periodograms over the years. The estimate of the spectra is further smoothed by applying a 1-2-1 filter 30 times in the frequency domain. This smooths the signal over around 15 points, yielding a spectral resolution of around 4.10^{-2} cpd.

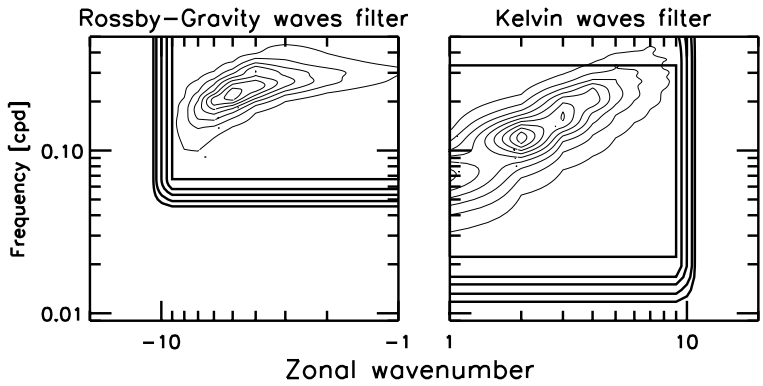

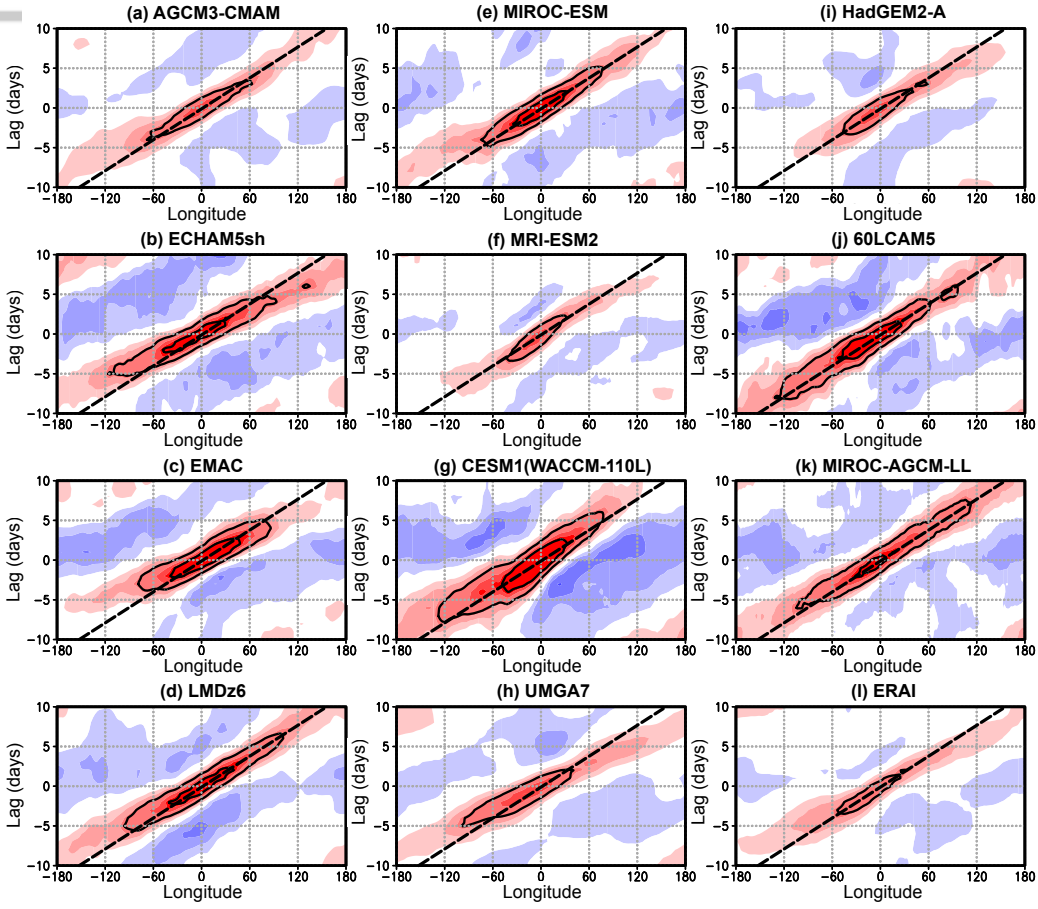

FIGURE 7 Time evolution of the zonal wind anomaly at the equator due to the passage of Kelvin waves at 50 hPa. The contour interval is 1.5 m s^{-1}, and blue colors are negative values. Values of 5 m s^{-1} and 10 m s^{-1} are highlighted by the black contours; the zero wind line is not shown. The thick dashed line represents the expected average uniform displacement (~20 m s^{-1}).

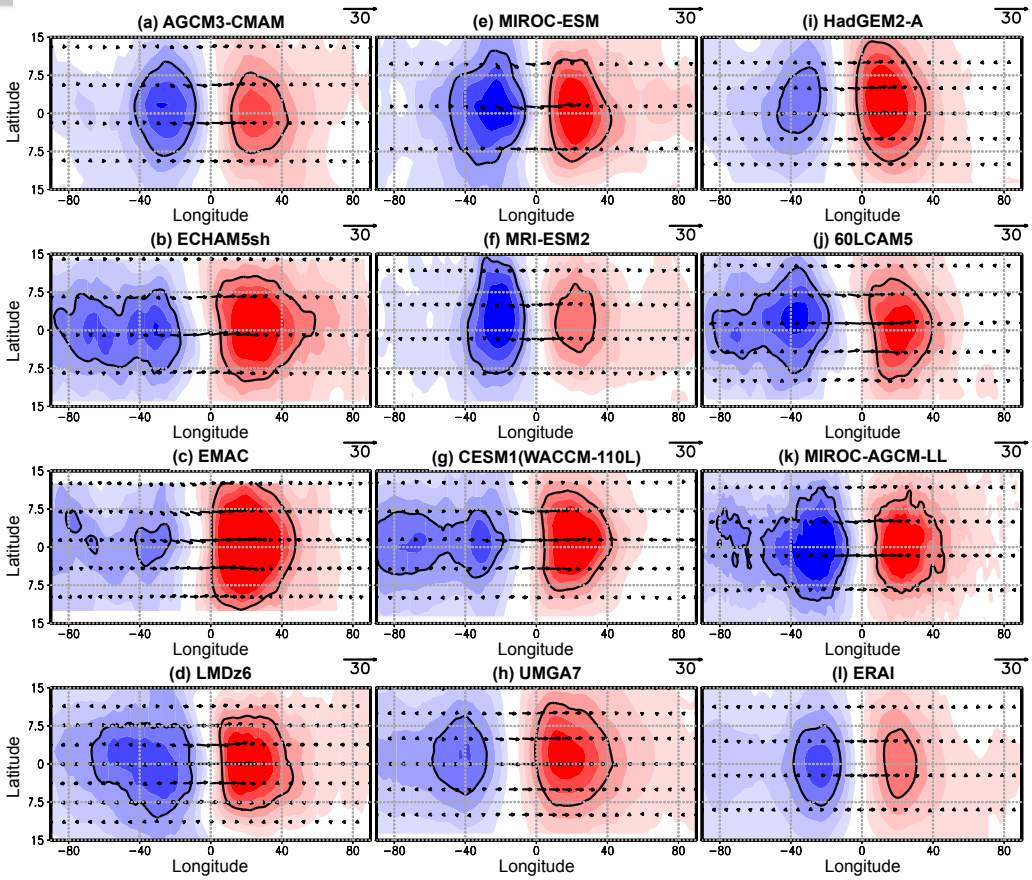

FIGURE 8 Longitude-latitude composite maps of winds and temperature anomalies due to Kelvin waves at 0-day lag and at 50hPa. The contours are for temperature with a contour interval of 0.5 K, and the 0 K line is not shown. The contours -2 K and 2 K are highlighted by the thick solid contours. A value of 20 m s^{-1} for the wind arrows is indicated by the arrows above each panel to the right and is identical for all panels.

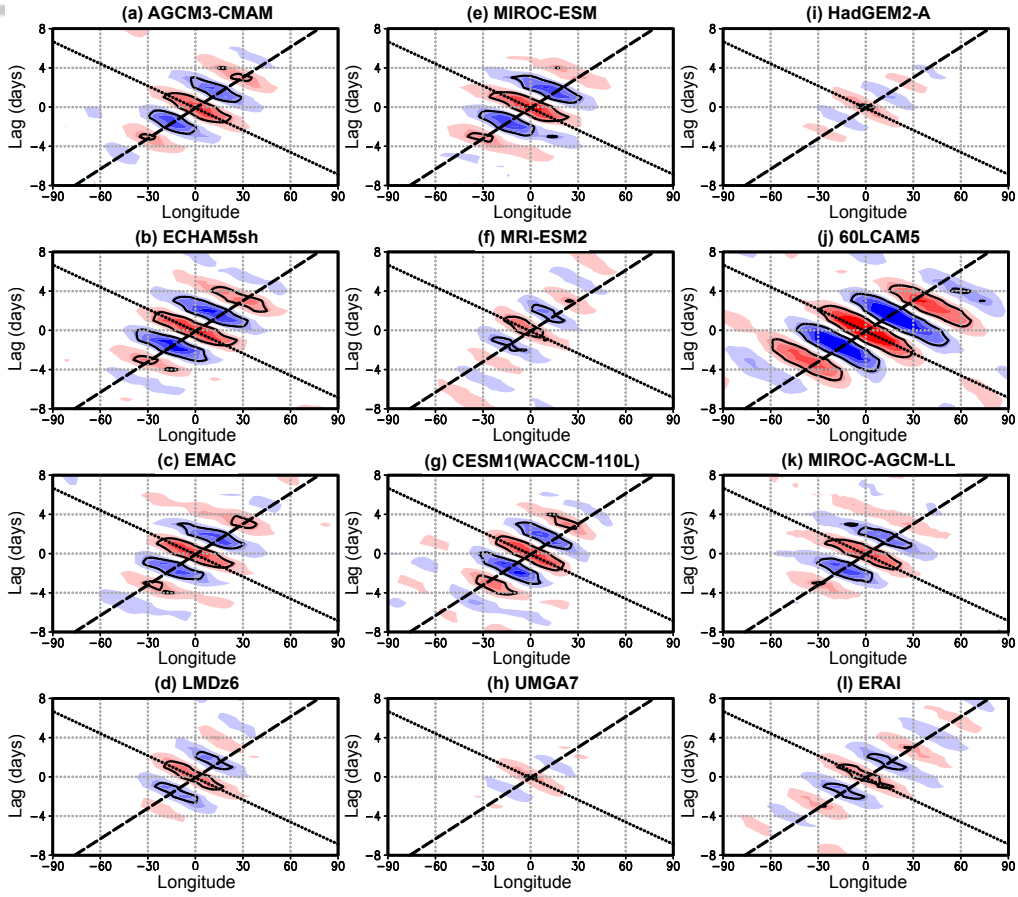

FIGURE 9 Time evolution of the meridional wind anomaly at the equator due to the passage of MRG waves at 50 hPa. The contour interval is 1 m s^{-1}, and the 0 m s^{-1} line is not shown. The blue colors represent negative values. Values of -2.5 m s^{-1} and 2.5 m s^{-1} are shown with the black solid contours. The dotted and dashed lines are for horizontal displacement at the speeds of ± 13 m s^{-1} respectively.

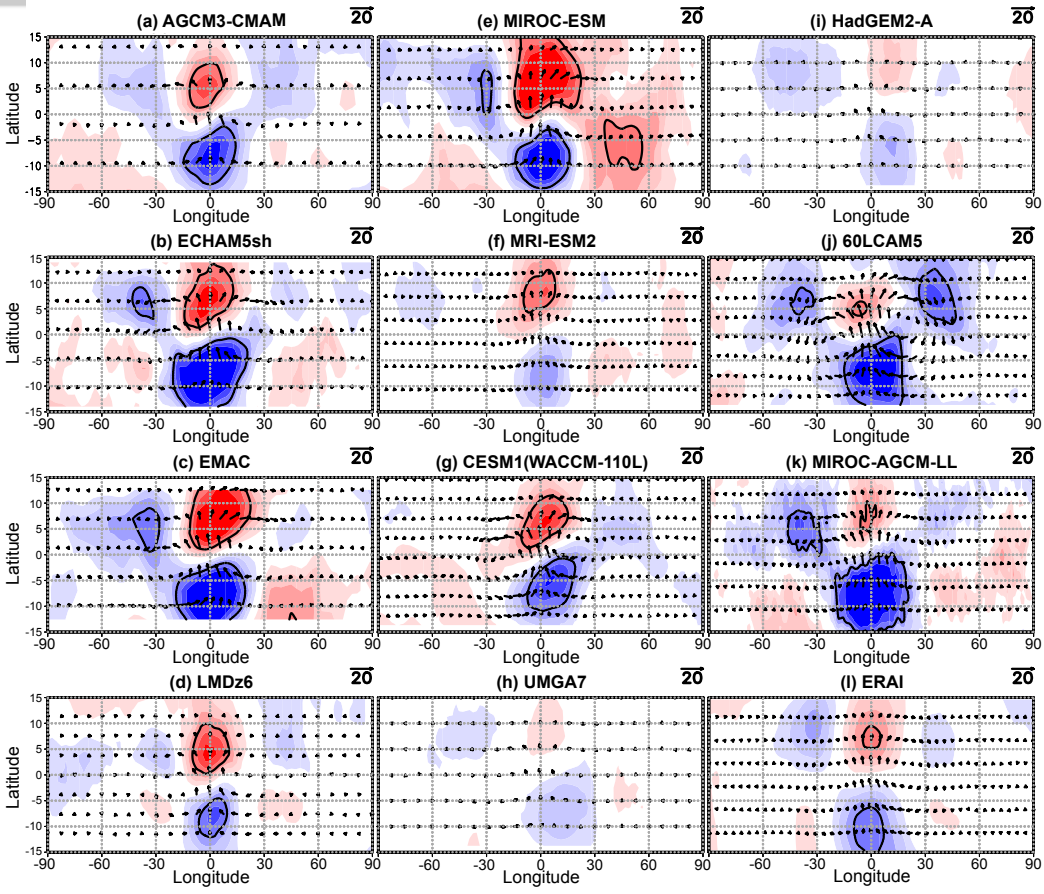

FIGURE 10 Longitude-latitude composite maps of winds and temperature anomalies for the MRG waves at 0-day lag and at 50 hPa. The contours are for temperature with a contour interval of 0.25 K, and the 0 K line is not shown. Values of -1K and 1K are highlighted by the solid black contours. A value of 20 m s^{-1} for the wind arrows is indicated by the arrows above each panel to the right and is identical for all panels.

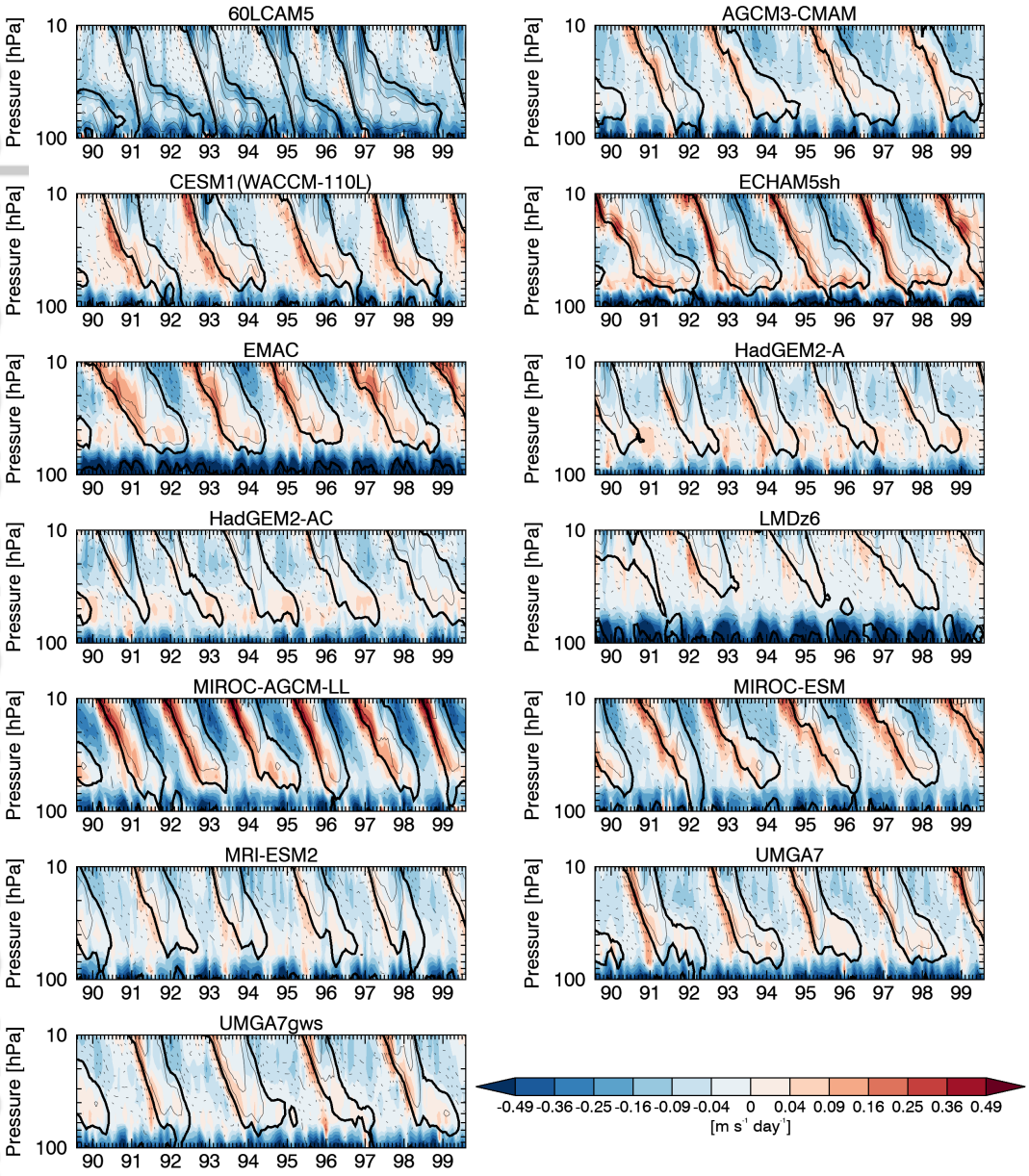

FIGURE 11 Zonal-mean zonal acceleration due to EP flux divergence from all resolved waves in the QBOi models as a function of pressure and time averaged over 10°S–10°N. Time runs from January 1990 to December 1999. Zonal-mean zonal winds are overplotted with black contours with positive winds represented by solid lines and negative winds represented by dotted lines. The thick black line is the zero-wind line, and the contour interval is 5.7 m s^{-1}

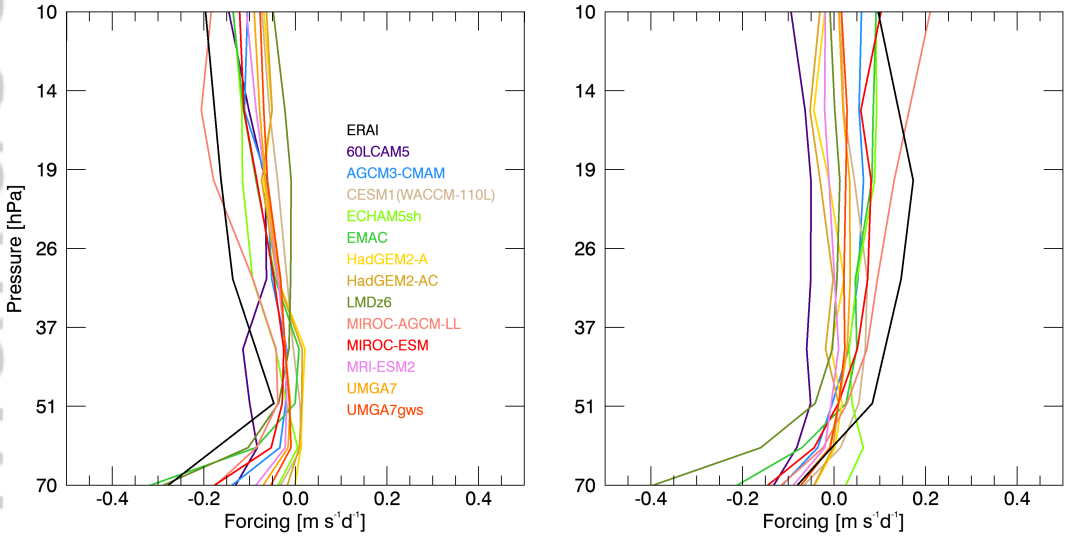

FIGURE 12 Zonal-mean zonal acceleration due to resolved waves in the QBOi models and the total zonal-mean zonal force required to drive the observed QBO estimated from LHS of Equation 3 using ERAI data. The profiles are averaged over periods in the 30 year datasets when there are westward (left) and eastward (right) shear zones. Westward shear zones are defined as when the vertical shear of the zonal-mean zonal wind is negative, and eastward shear zones are defined as when the vertical shear of the zonal-mean zonal wind is positive. Averaged over 10°S–10°N

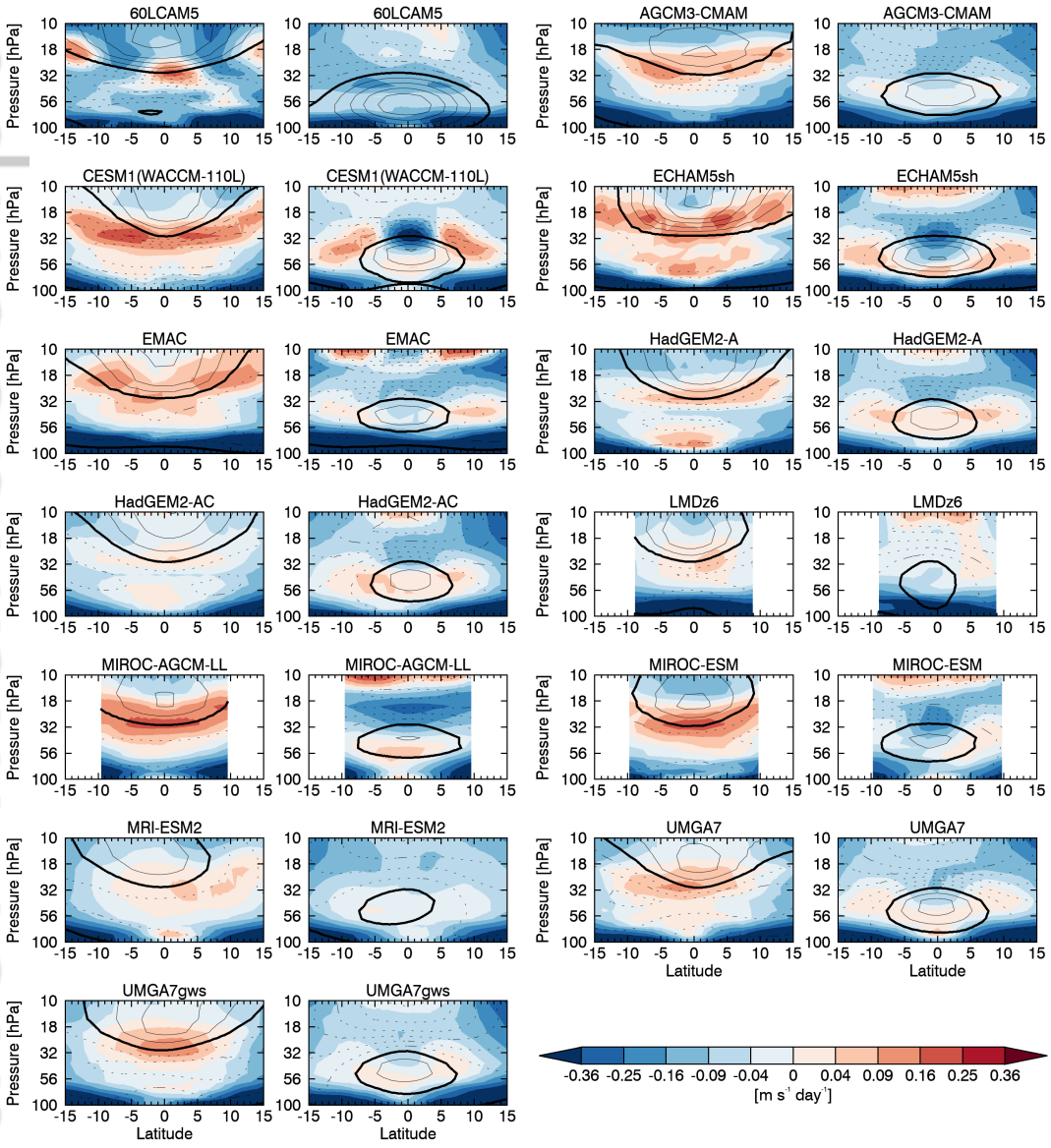

FIGURE 13 Latitude-altitude distribution of the resolved wave forcing averaged over the periods in the 30 year simulations of descending eastward (left of each model pair) and descending westward (right of each model pair) phases of the QBO. Zonal-mean zonal wind is overplotted with the black contours with positive winds represented by solid lines and negative winds represented by dotted lines. The thick black line is the zero-wind line, and the contour interval is 5 m s^{-1}.

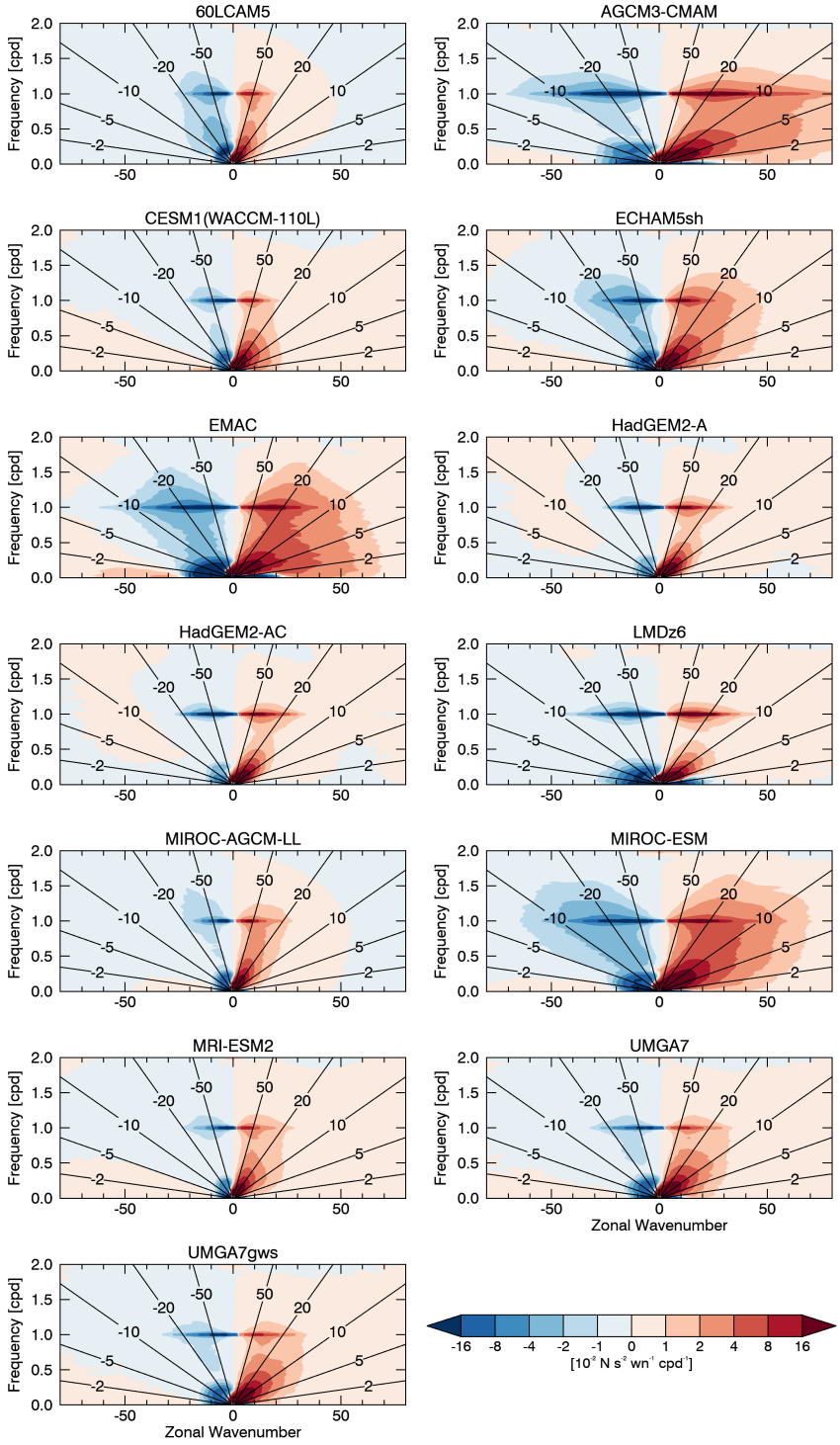

FIGURE 14 Wavenumber-frequency distribution of the vertical component of EP flux (F_p) averaged over 70–80 hPa and 10°S–10°N. Phase speed lines are overplotted in black. Westward propagating waves are represented by negative flux and eastward propagating waves are represented by positive flux. The spectra are based on 10 years of 6-hourly data except for UMGA7 and UMGA7gws, which are based on 6 years of 6-hourly data.

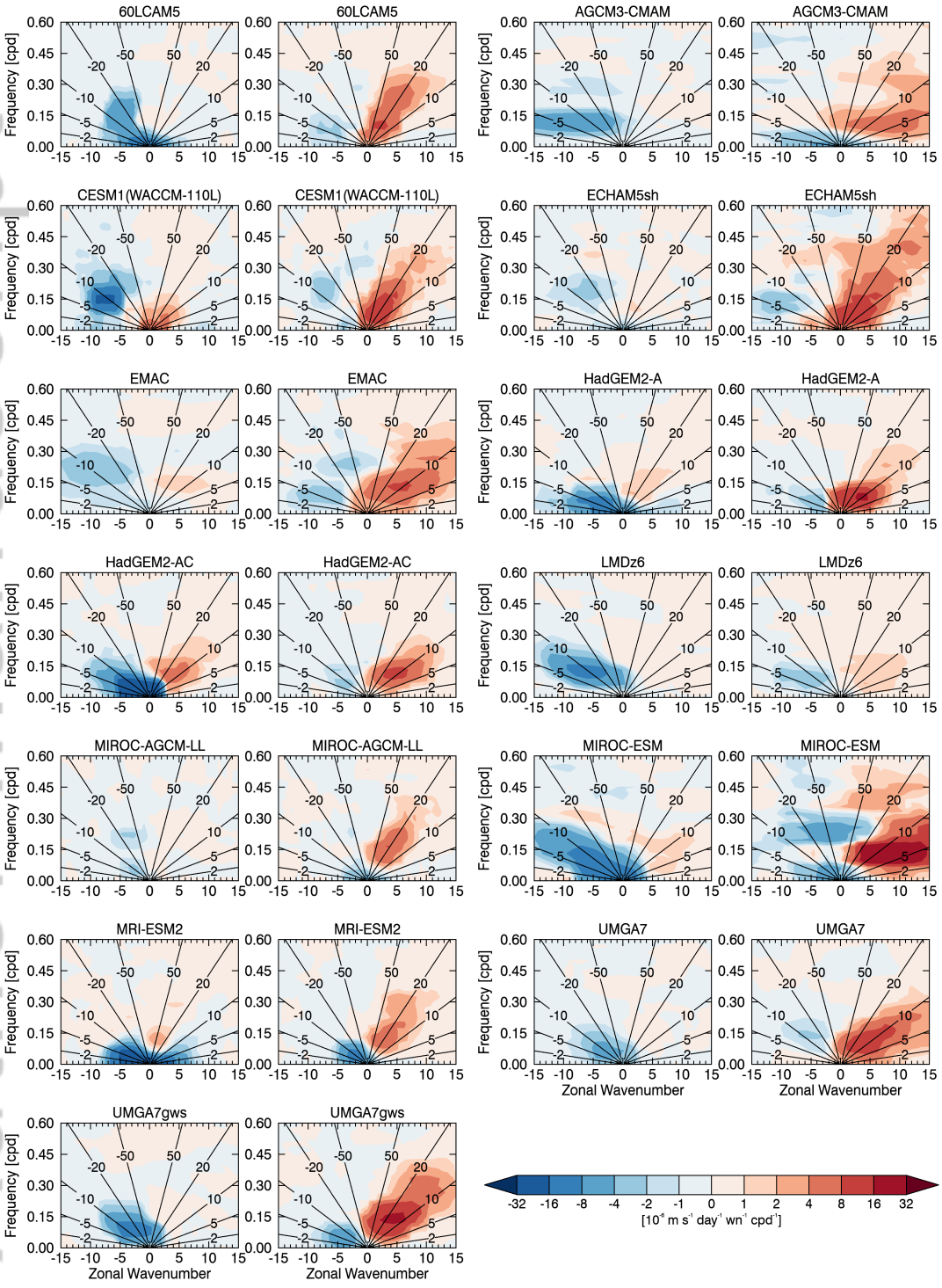

FIGURE 15 Wavenumber-frequency distribution of the resolved wave forcing in 10^{-6} m s^{-1}day^{-1} near 25 hPa averaged over 10°S–10°N for westward QBO shear zones (left of each model pair) and eastward QBO shear zones (right of each model pair). Phase speed lines are overplotted in black. Westward propagating waves are represented by negative forcing and eastward propagating waves are represented by positive forcing.

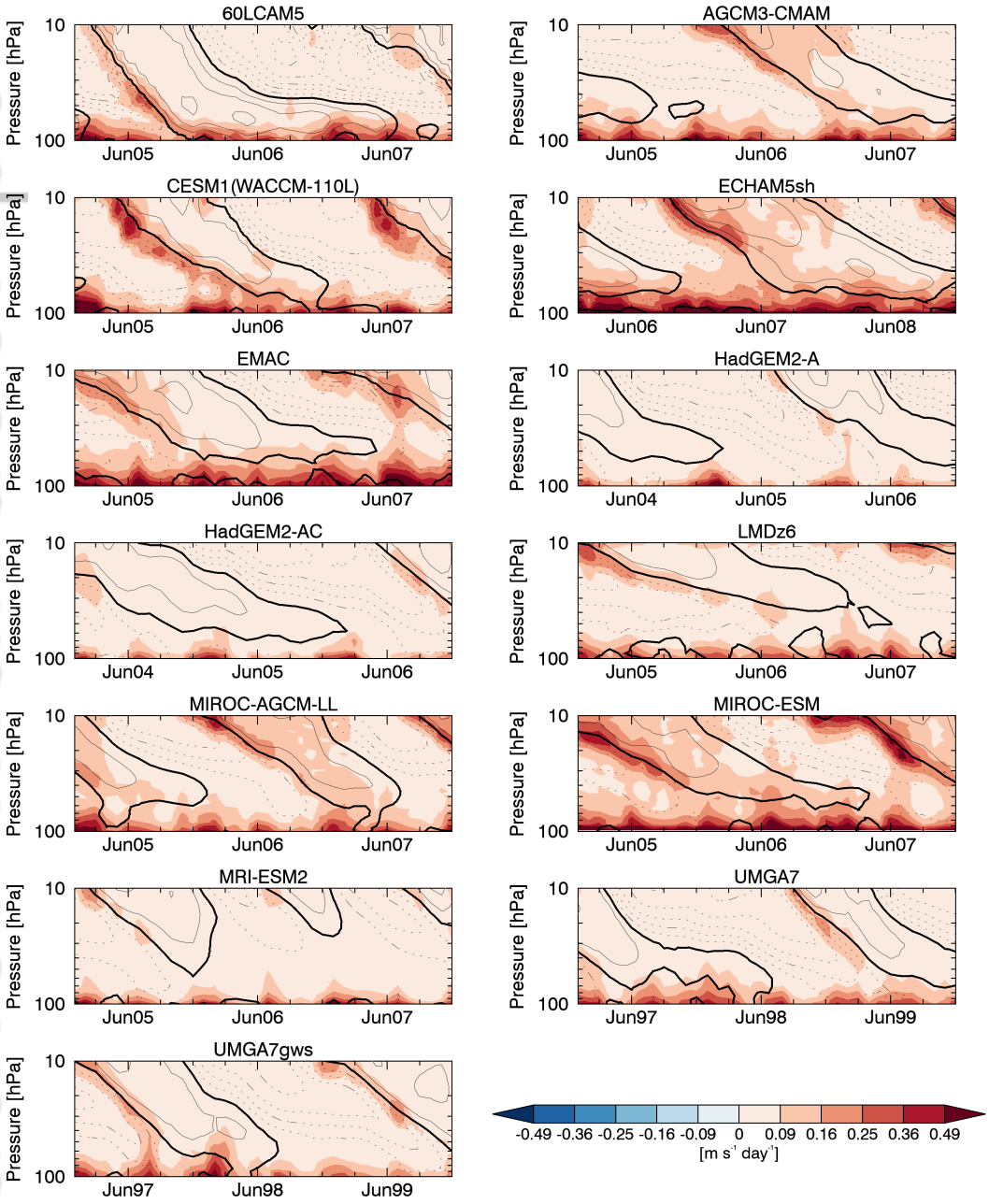

FIGURE 16 Contribution to zonal-mean zonal acceleration from large-scale eastward propagating (Kelvin) waves as a function of pressure and time averaged over 10°S–10°N. Zonal-mean zonal winds are overplotted with black contours with positive winds represented by solid lines and negative winds represented by dotted lines. The thick black line is the zero-wind line, and the contour interval is 6.7 m s^{-1}.

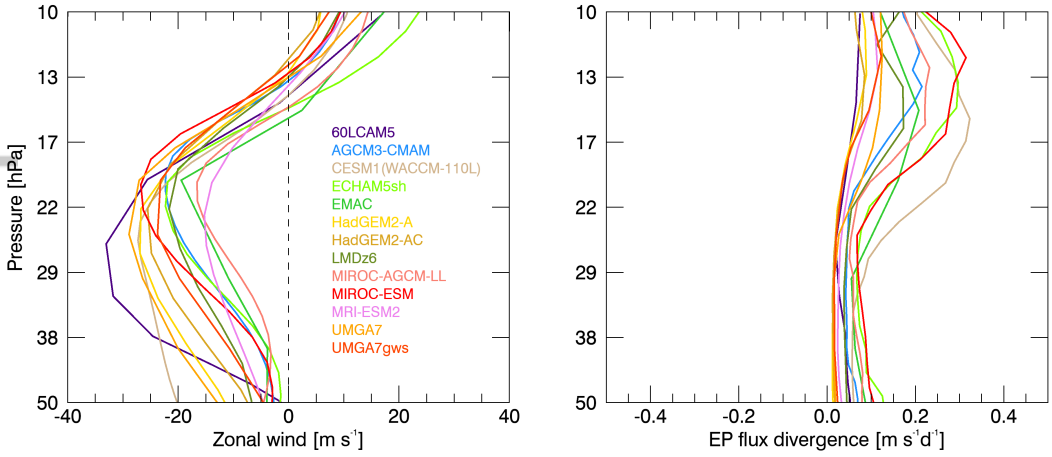

FIGURE 17 Zonal-mean zonal wind profiles (left) and zonal acceleration (wave forcing) due to large-scale eastward propagating waves (right) averaged over 10°S–10°N for periods when the zero-wind line was between 17-13 hPa.

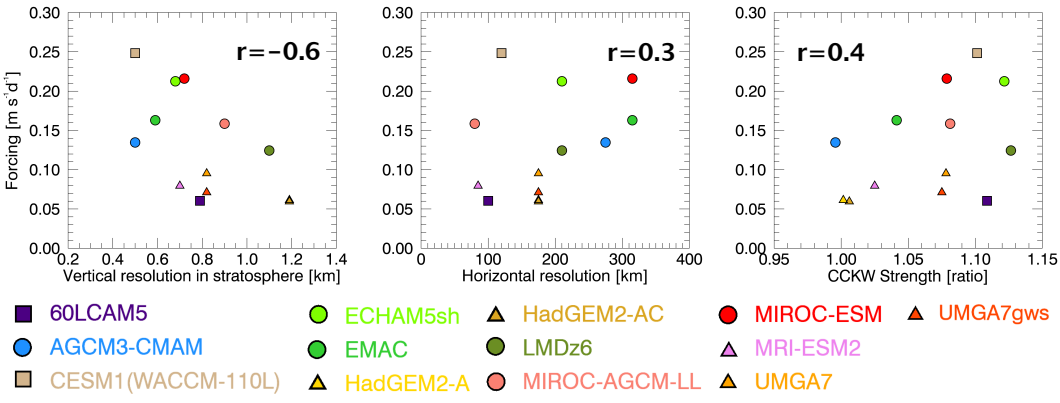

FIGURE 18 Zonal-mean zonal acceleration due to EP flux divergence from large-scale eastward propagating waves averaged over 26–10 hPa as a function of model vertical (left) and horizontal (center) resolution and strength of CCKWs (right). Model colors are given in Figure 17. Different symbols denote different dynamical core types. Circles are Eulerian/spectral transform, triangles are semi-Lagrangian/semi-implicit, and squares are either finite volume (CESM1(WACCM5-110L)) or spectral element (60LCAM5). Note that HadGEM2-A and HadGEM2-AC overlap. Pearson correlation coefficients are also shown in each panel.

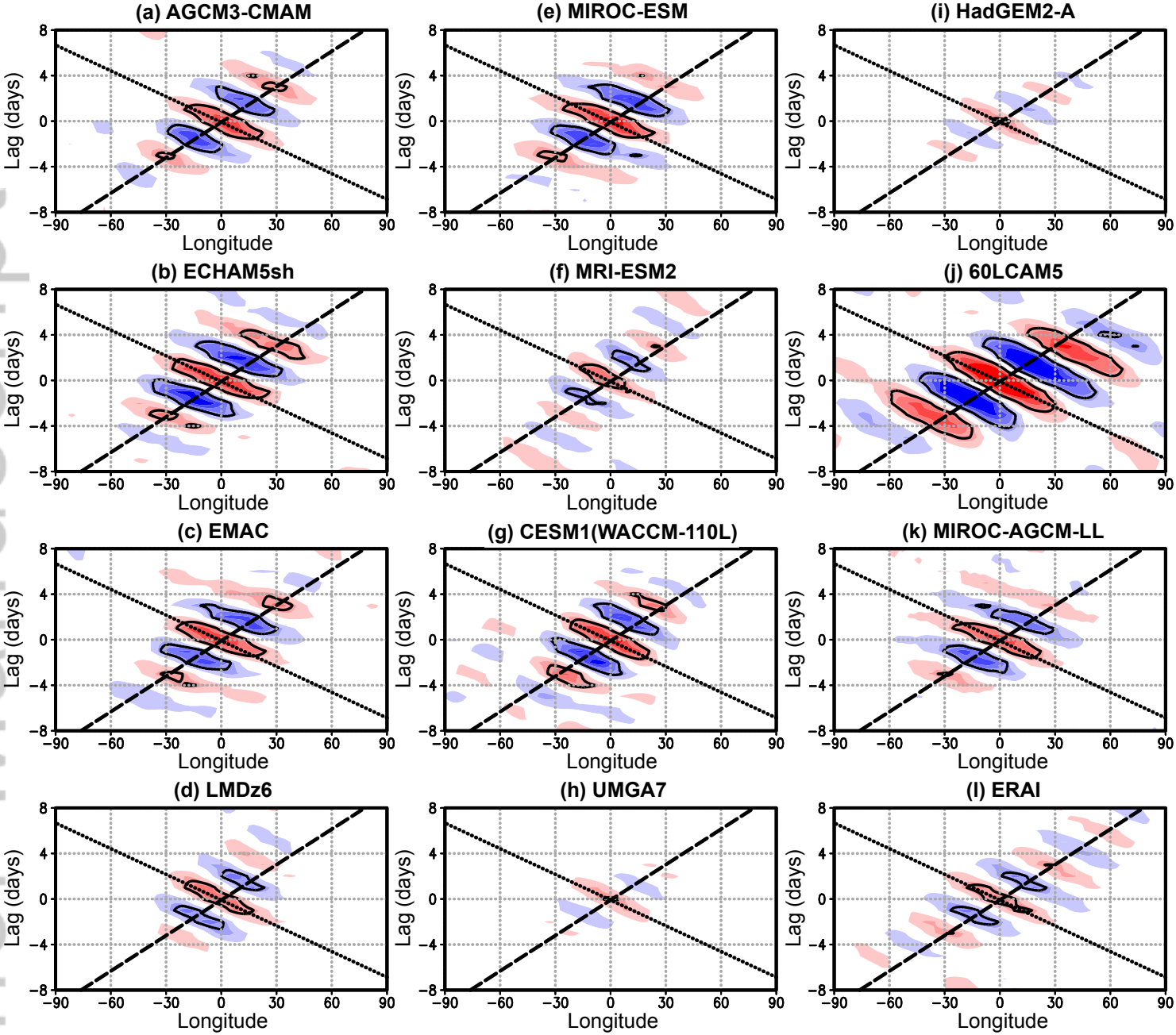
(a) AGCM3-CMAM
(e) MIROC-ESM
(i) HadGEM2-A
(b) ECHAM5sh
(f) MRI-ESM2
(j) 60LCAM5
(c) EMAC
(g) CESM1(WACCM-110L)
(k) MIROC-AGCM-LL
(d) LMDz6
(h) UMGA7
(l) ERAI
Lag (days)
Longitude
8
4
0
−4
−8
−90
−60
−30
0
30
60
90

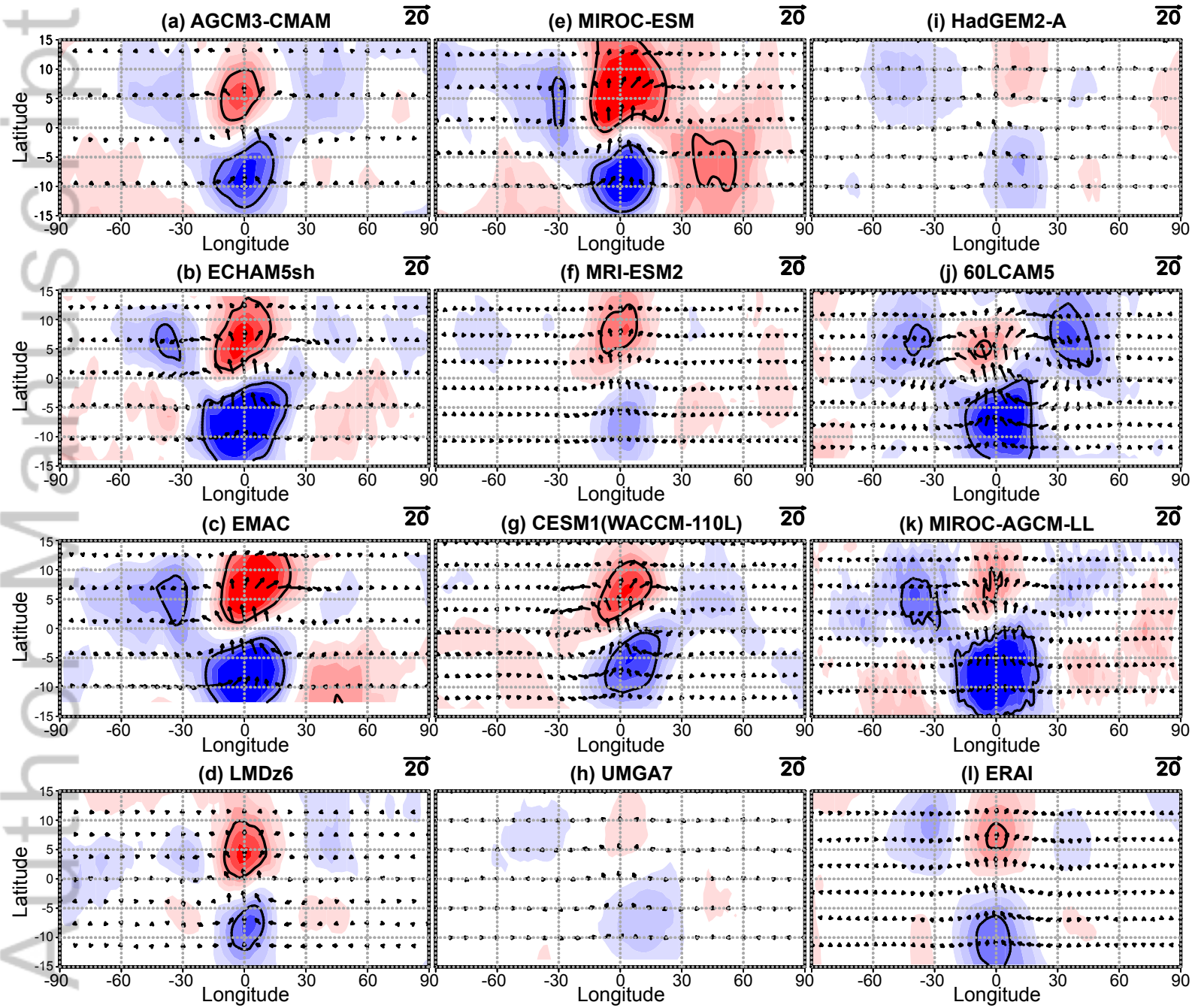
(a) AGCM3-CMAM
(e) MIROC-ESM
(i) HadGEM2-A
(b) ECHAM5sh
(f) MRI-ESM2
(j) 60LCAM5
(c) EMAC
(g) CESM1(WACCM-110L)
(k) MIROC-AGCM-LL
(d) LMDz6
(h) UMGA7
(l) ERAI
20
Latitude
Longitude
15
10
5
0
−5
−10
−15
−90
−60
−30
0
30
60
90

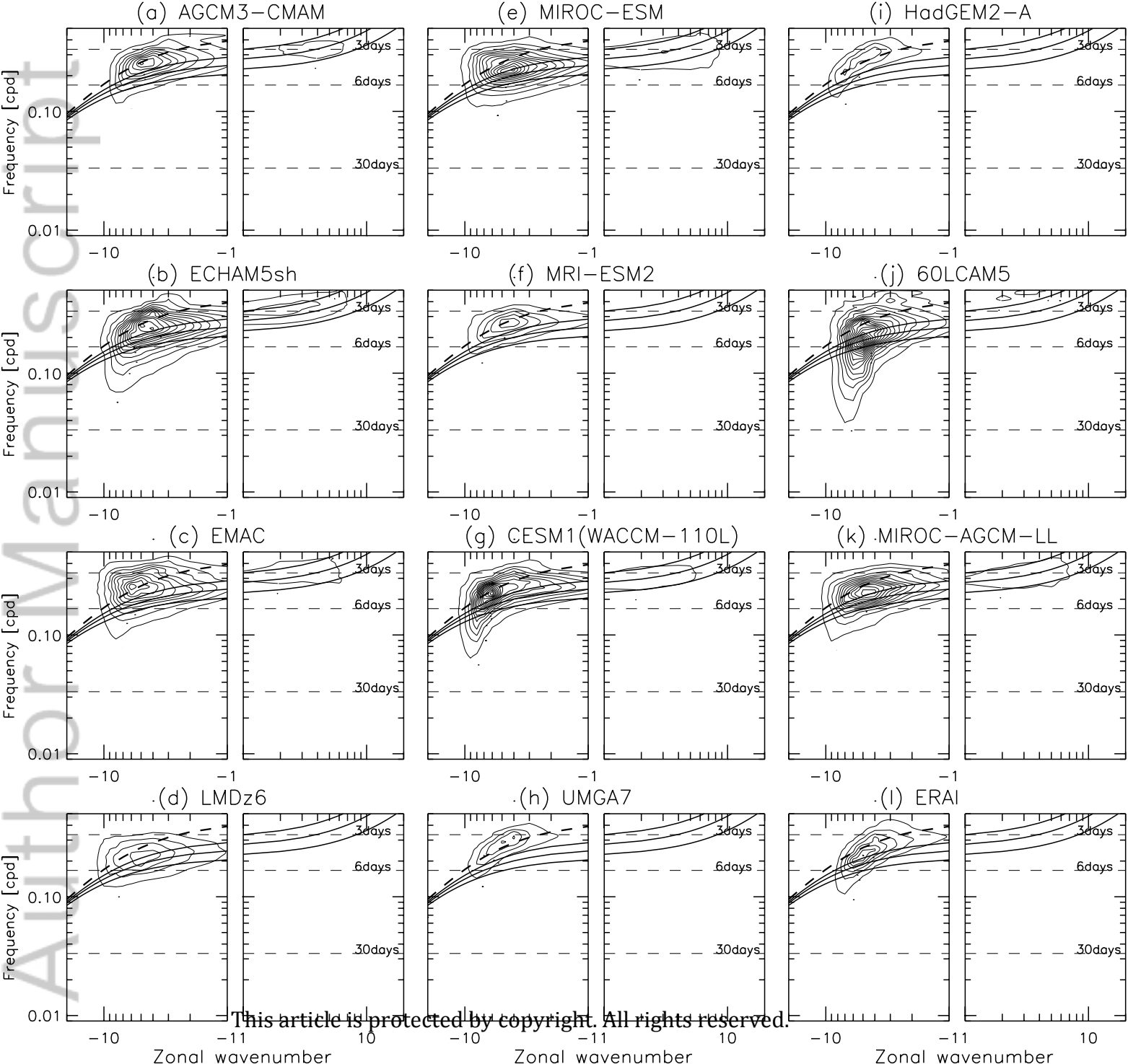

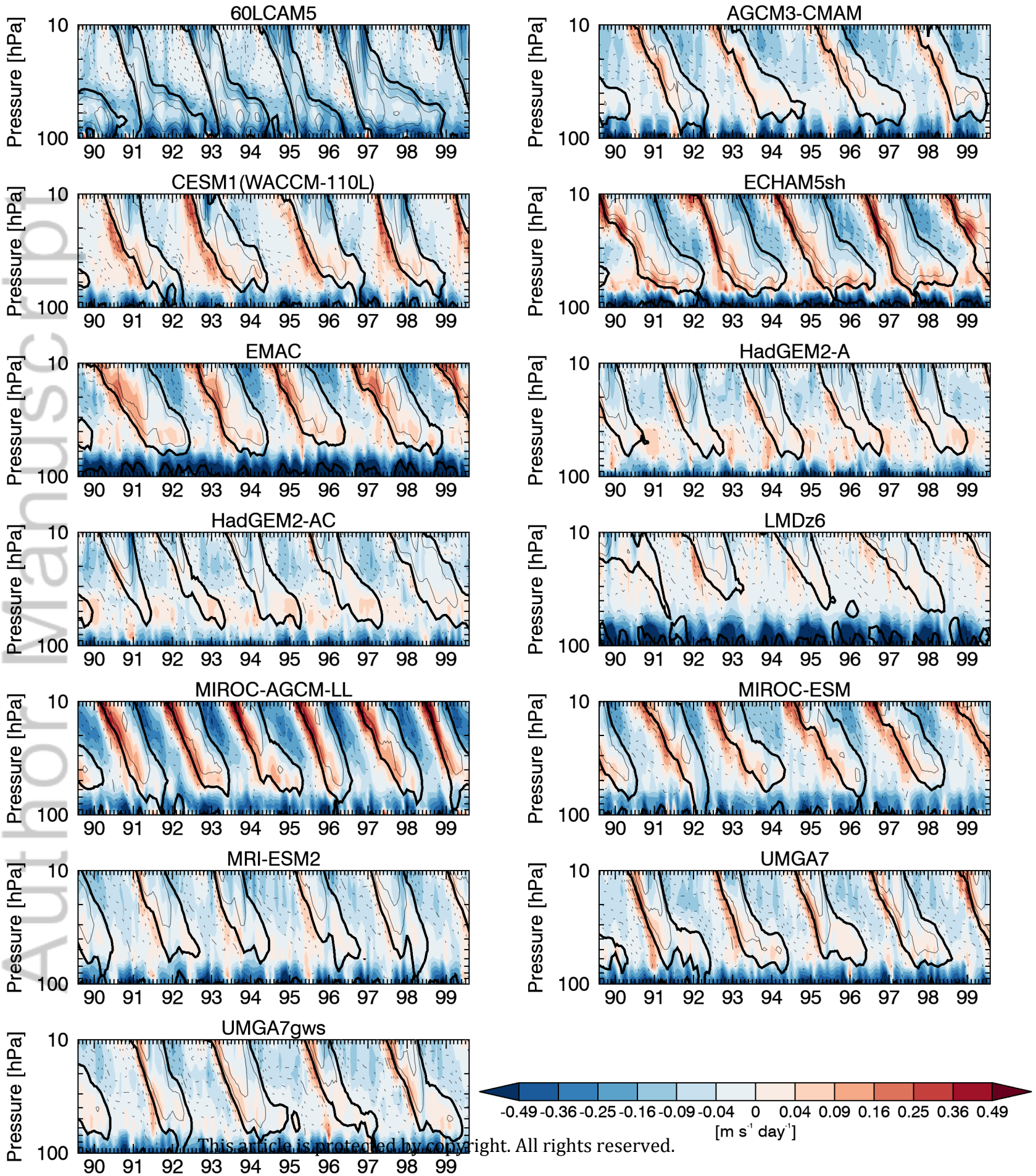

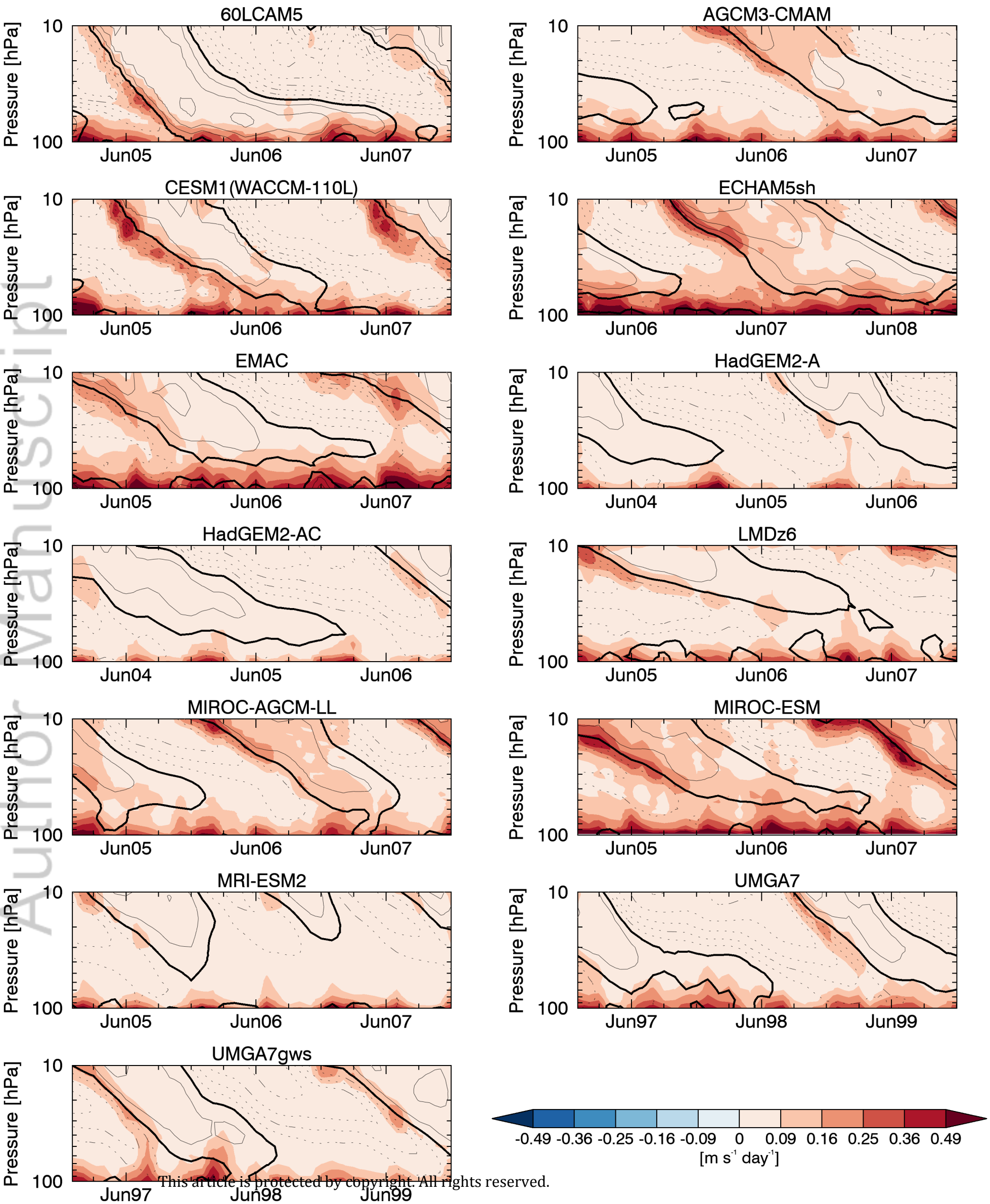

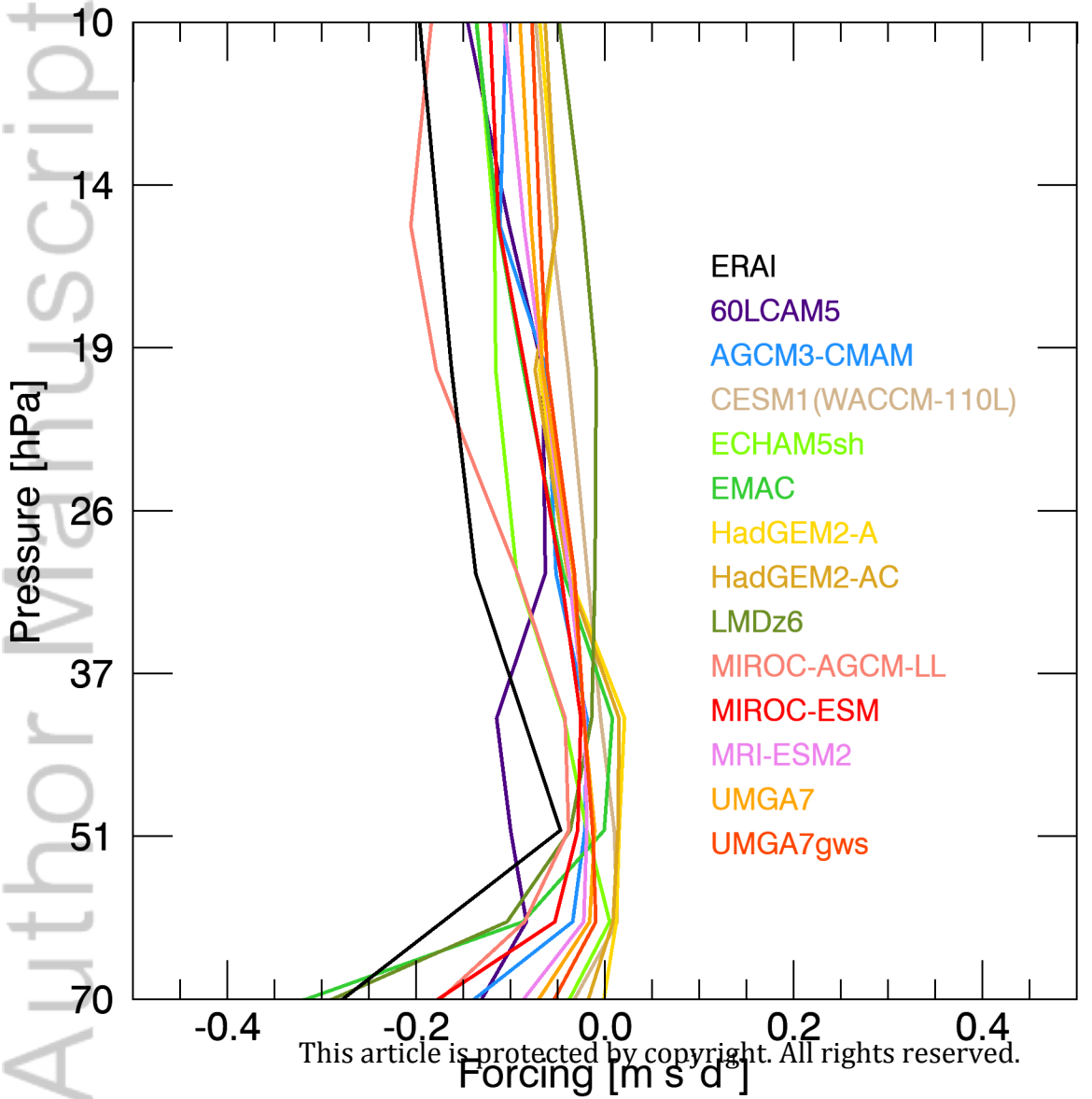

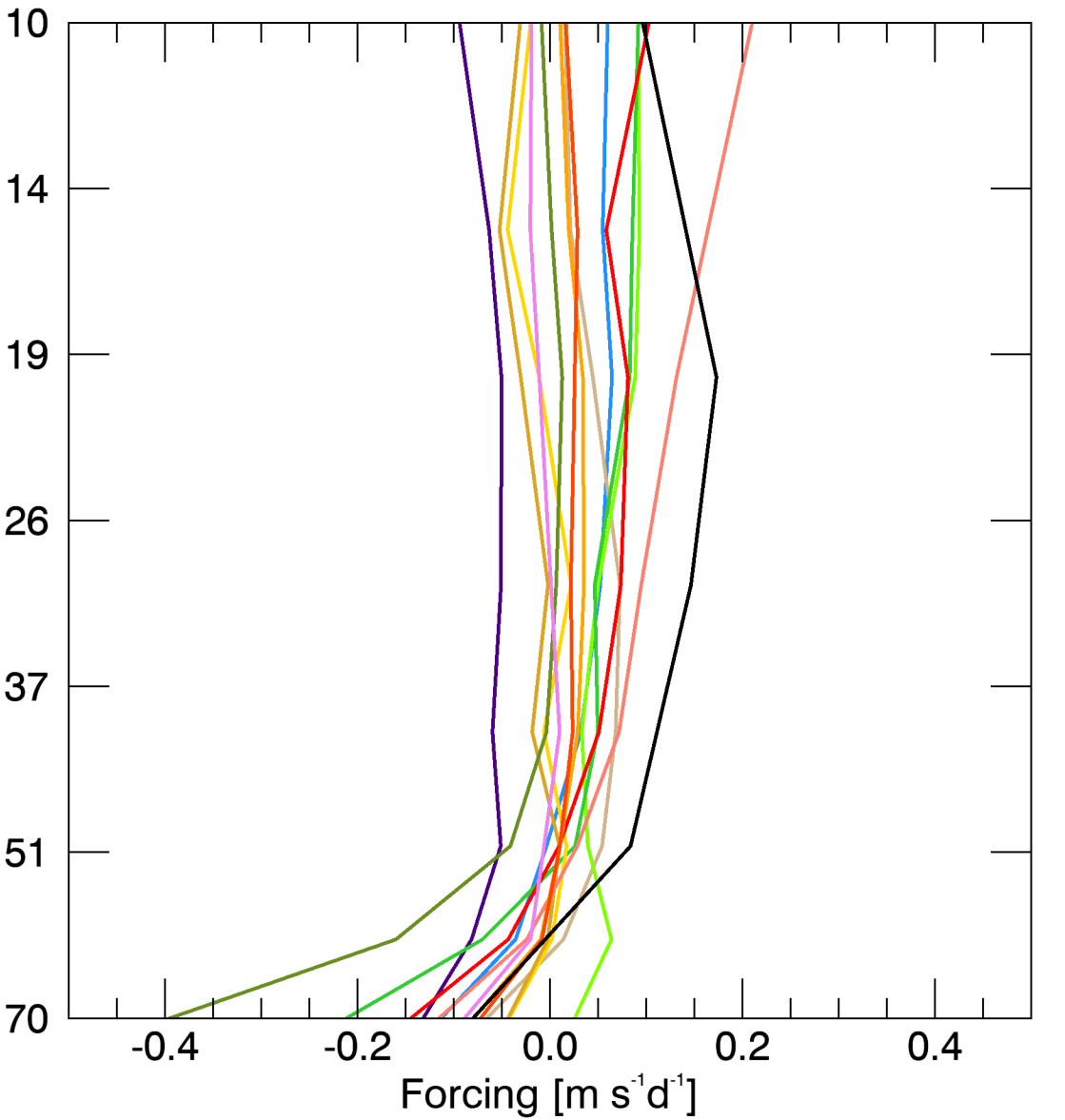

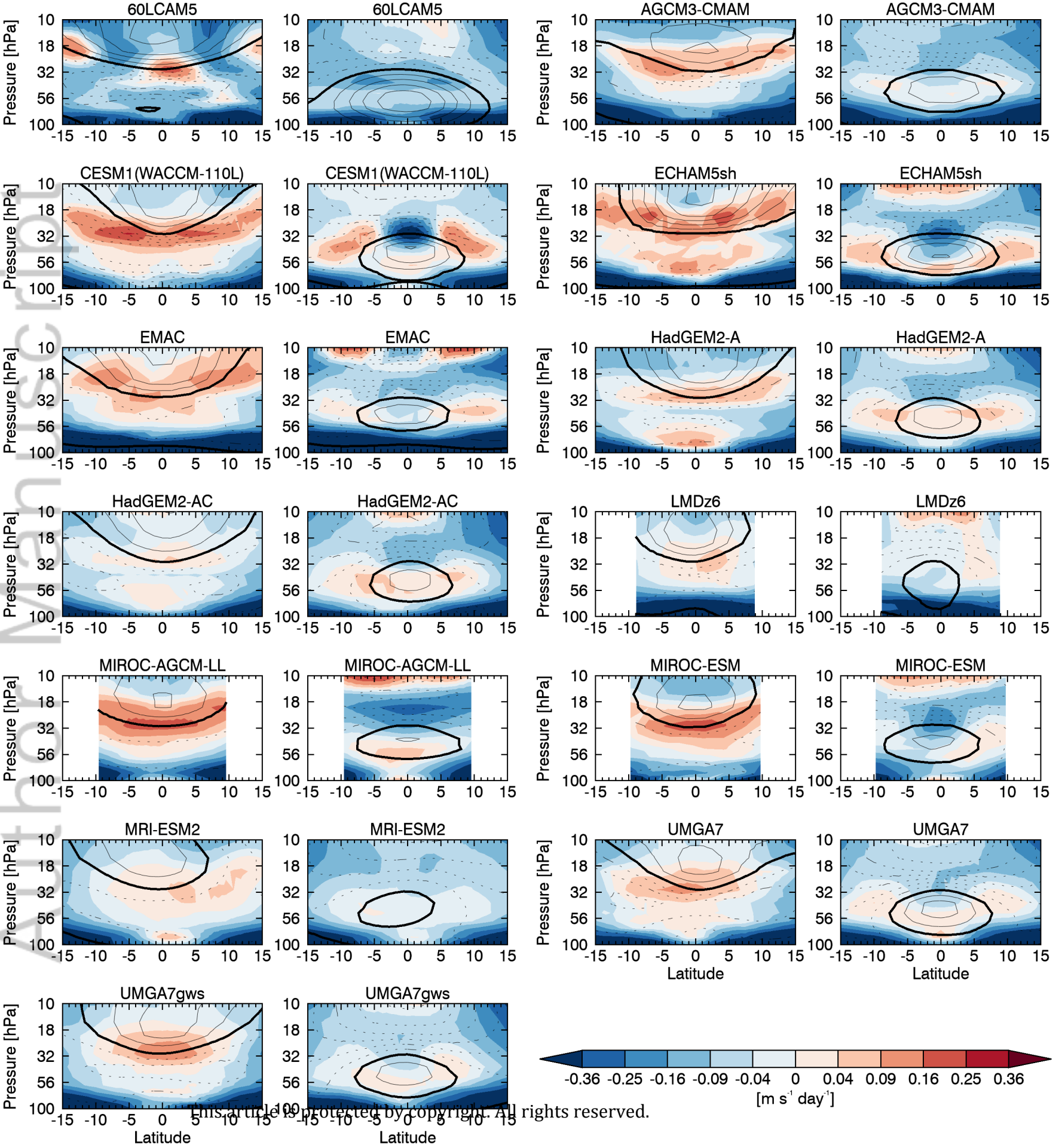

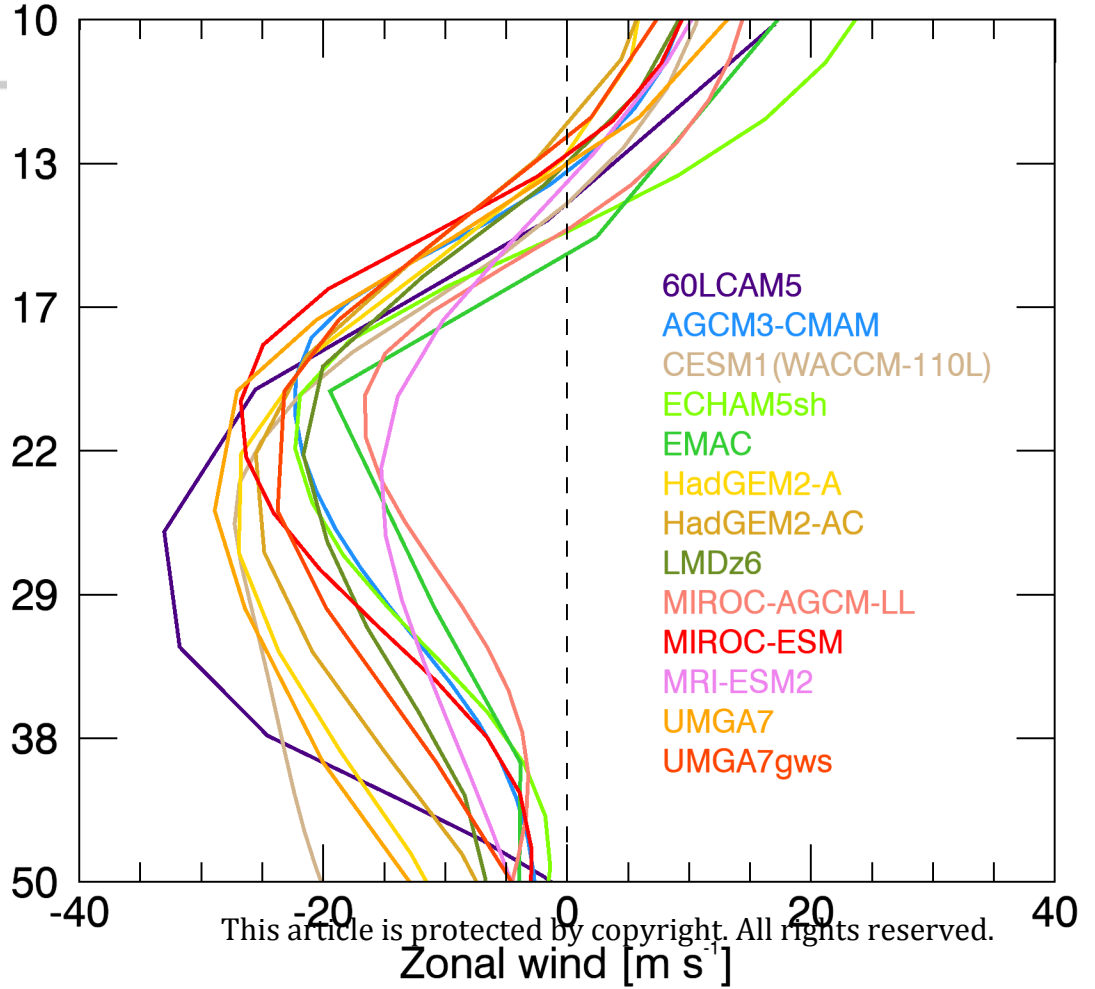

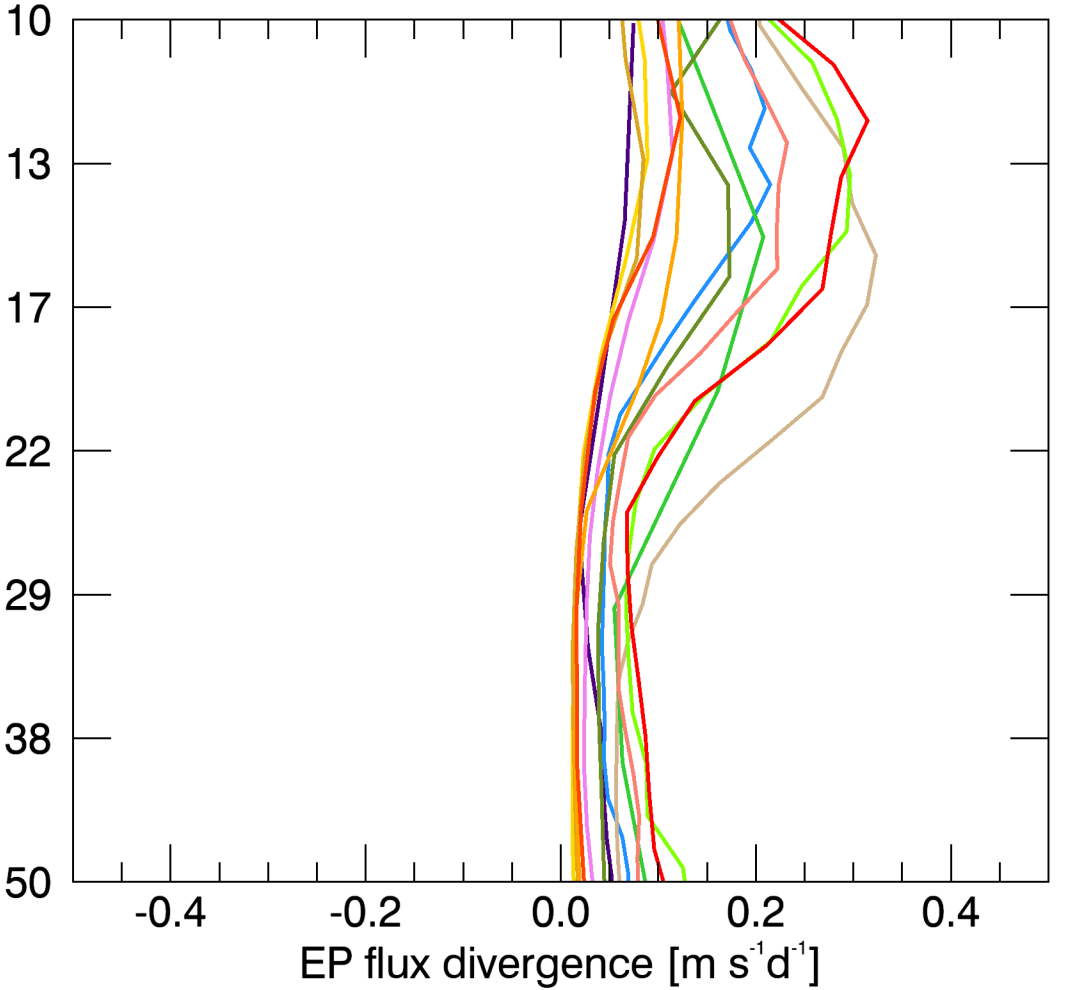

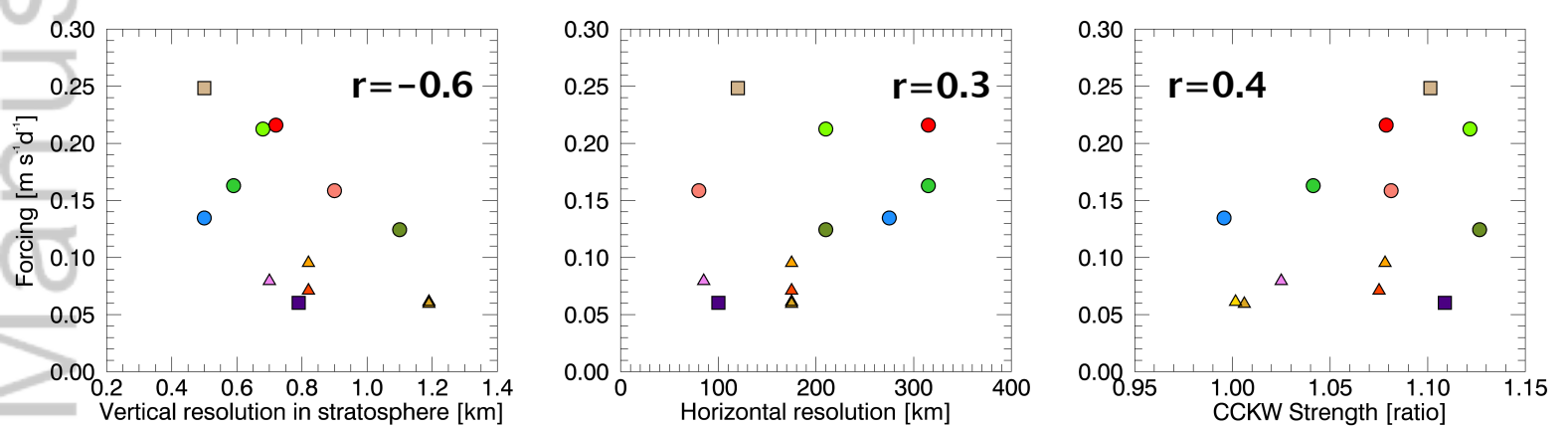
r=−0.6
r=0.3
r=0.4
Forcing [m s-1 d-1]
Vertical resolution in stratosphere [km]
Horizontal resolution [km]
CCKW Strength [ratio]
60LCAM5
AGCM3-CMAM
CESM1(WACCM-110L)
ECHAM5sh
EMAC
HadGEM2-A
HadGEM2-AC
LMDz6
MIROC-AGCM-LL
MIROC-ESM
MRI-ESM2
UMGA7
UMGA7gws

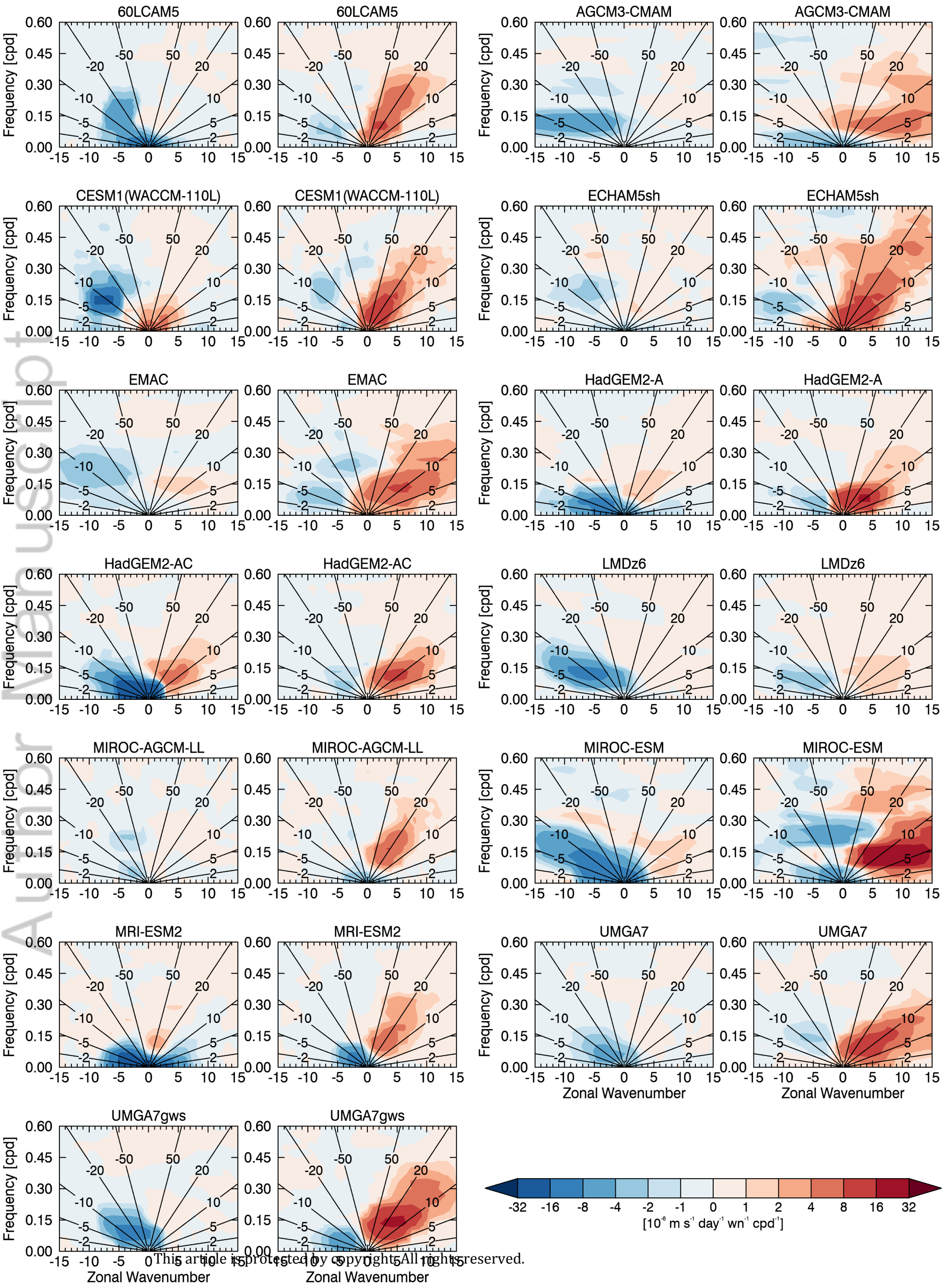

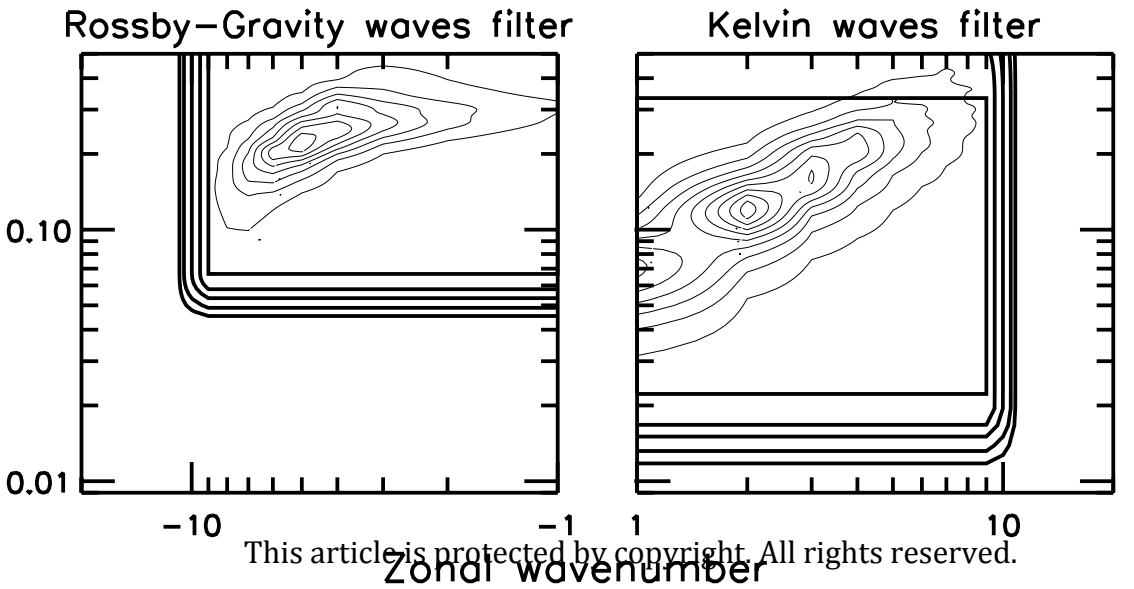

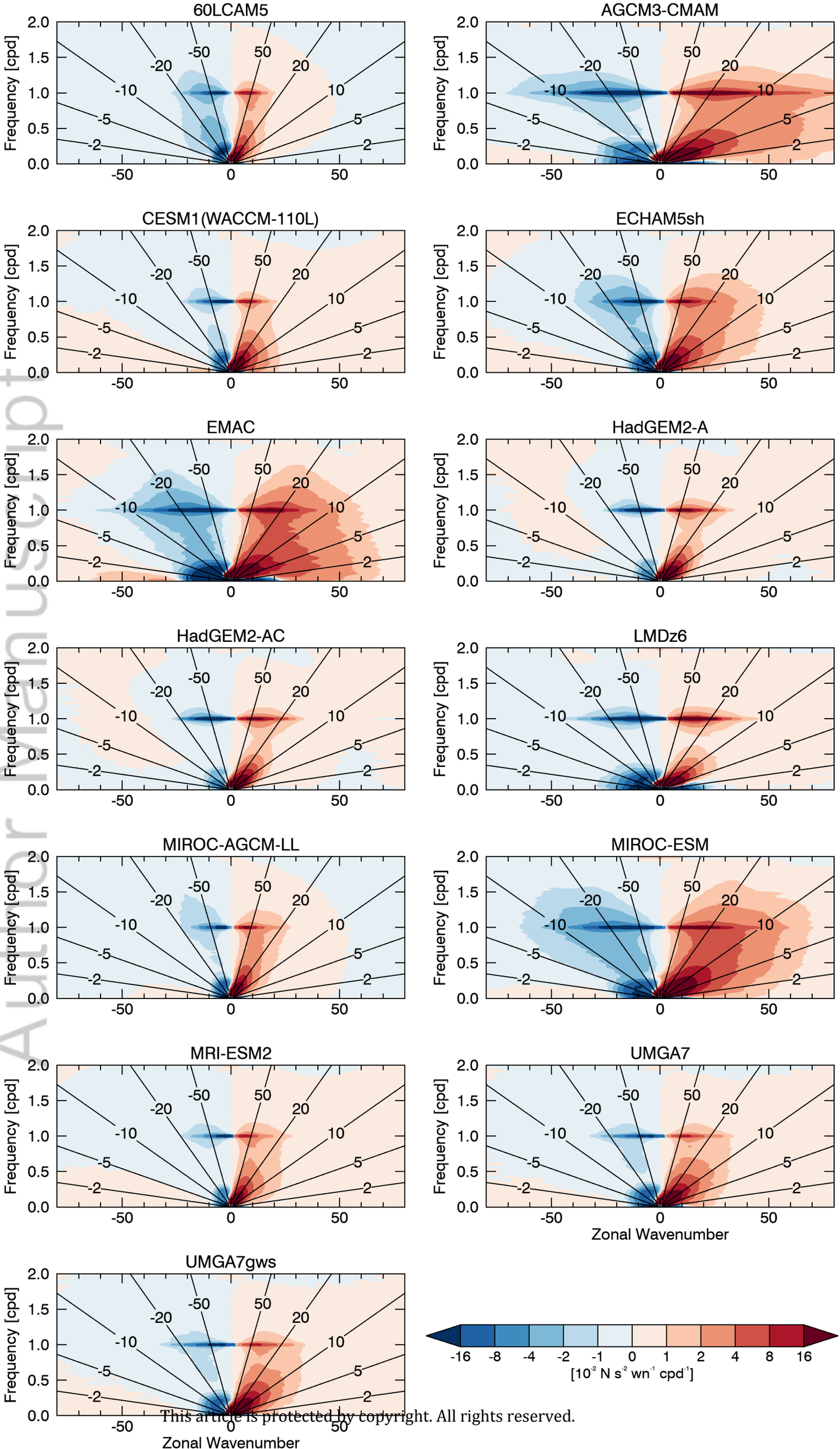

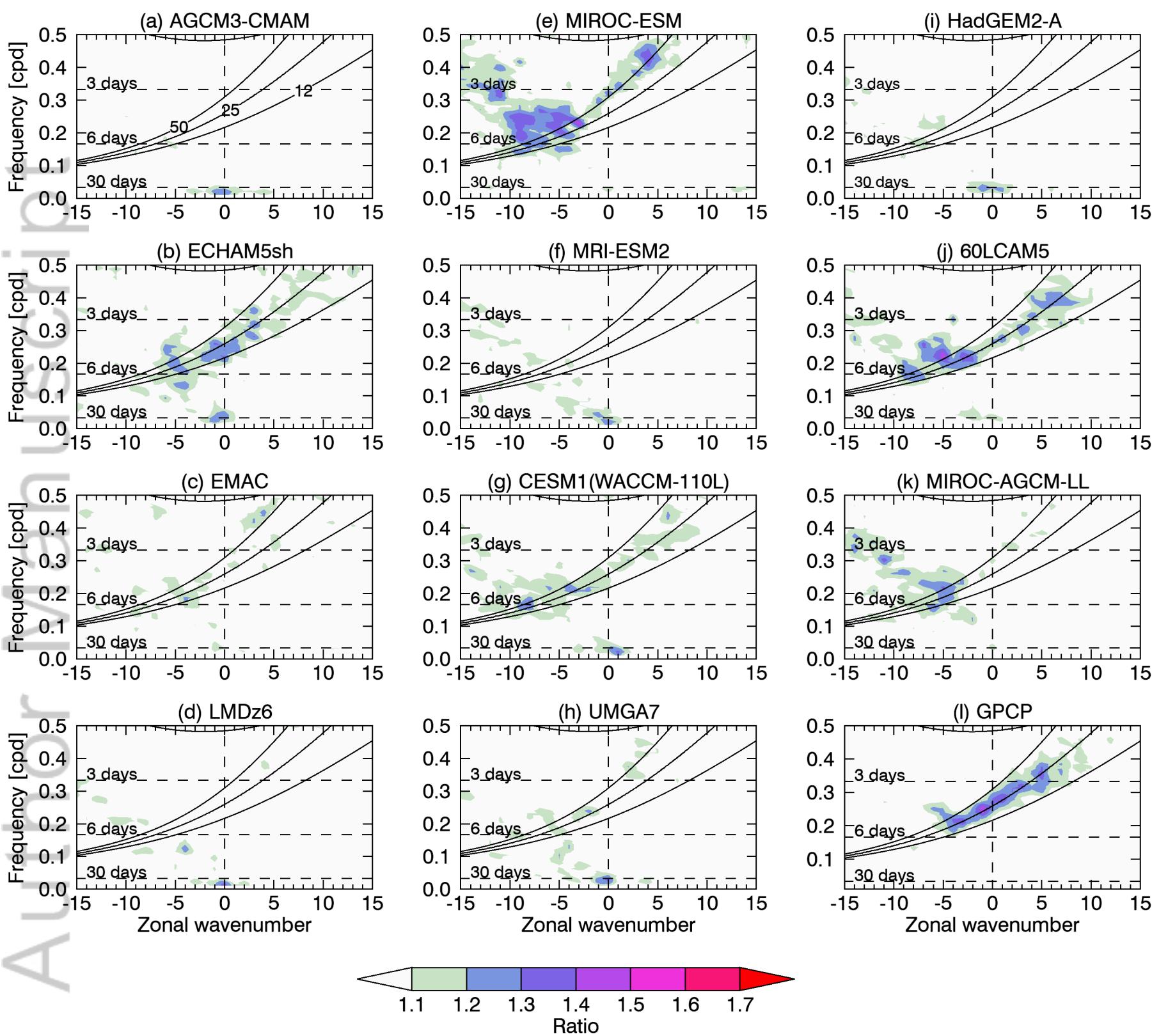

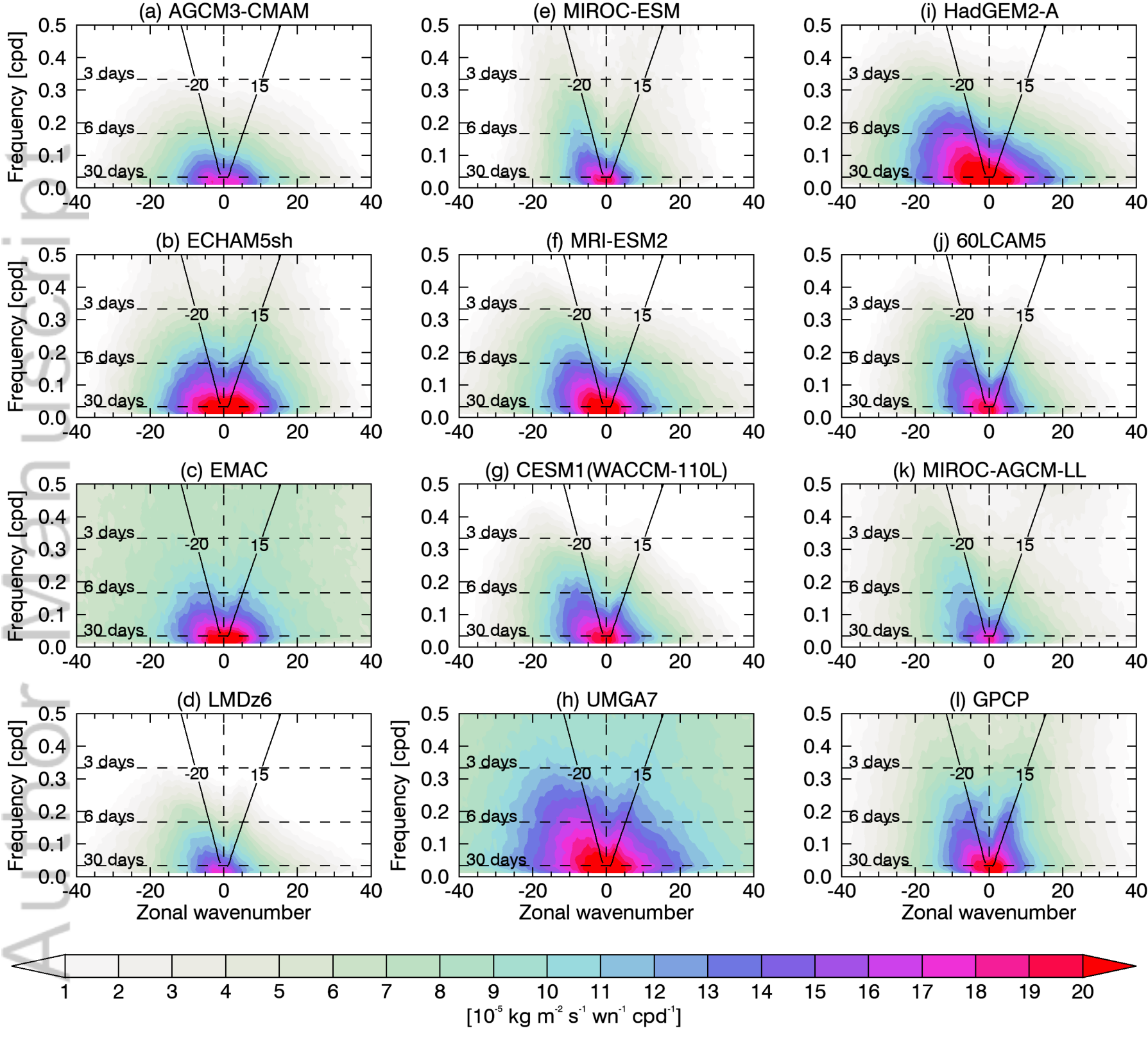

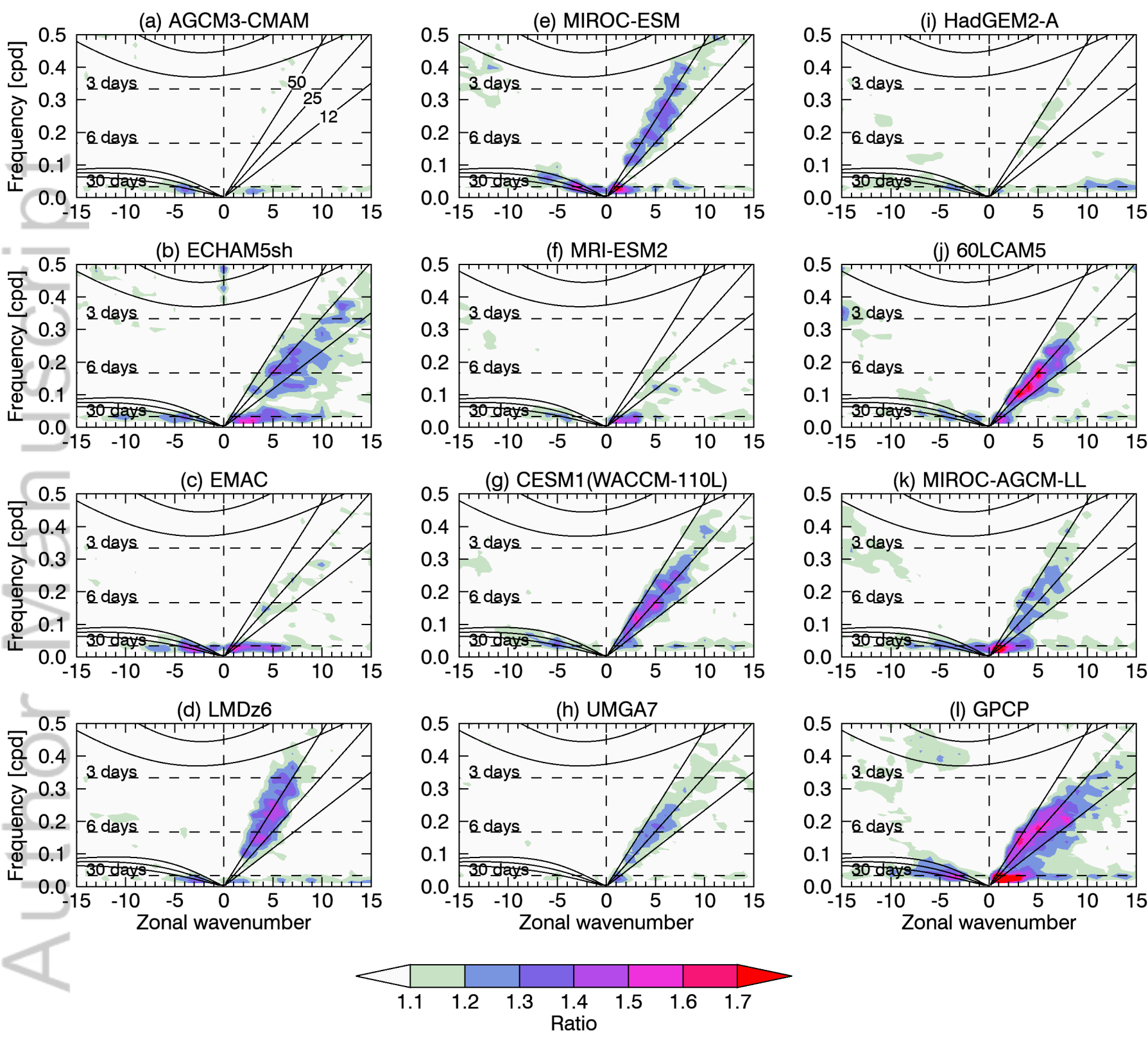

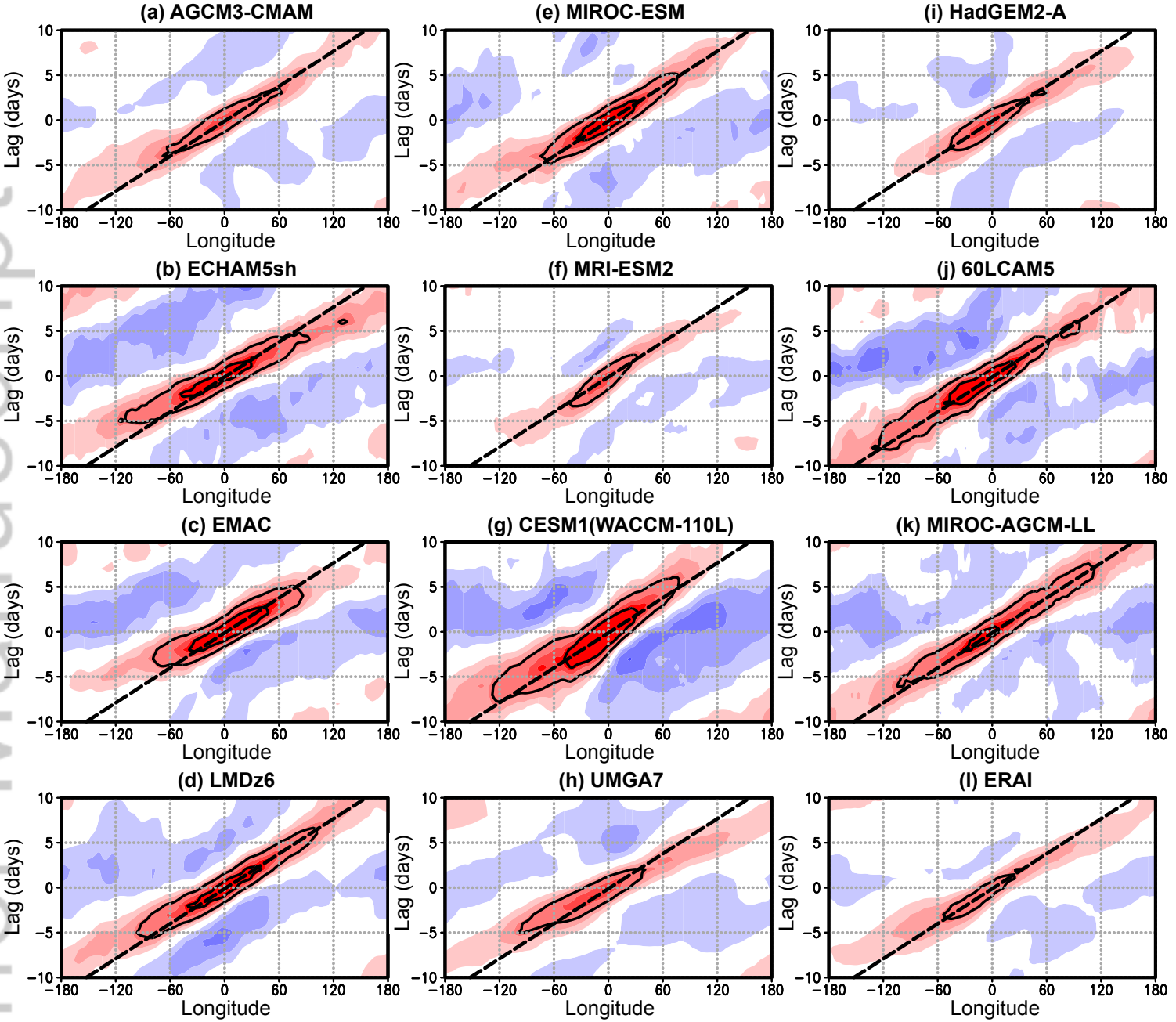
(a) AGCM3-CMAM
(e) MIROC-ESM
(i) HadGEM2-A
(b) ECHAM5sh
(f) MRI-ESM2
(j) 60LCAM5
(c) EMAC
(g) CESM1(WACCM-110L)
(k) MIROC-AGCM-LL
(d) LMDz6
(h) UMGA7
(l) ERAI
Lag (days)
Longitude
10
5
0
−5
−10
−180
−120
−60
0
60
120
180

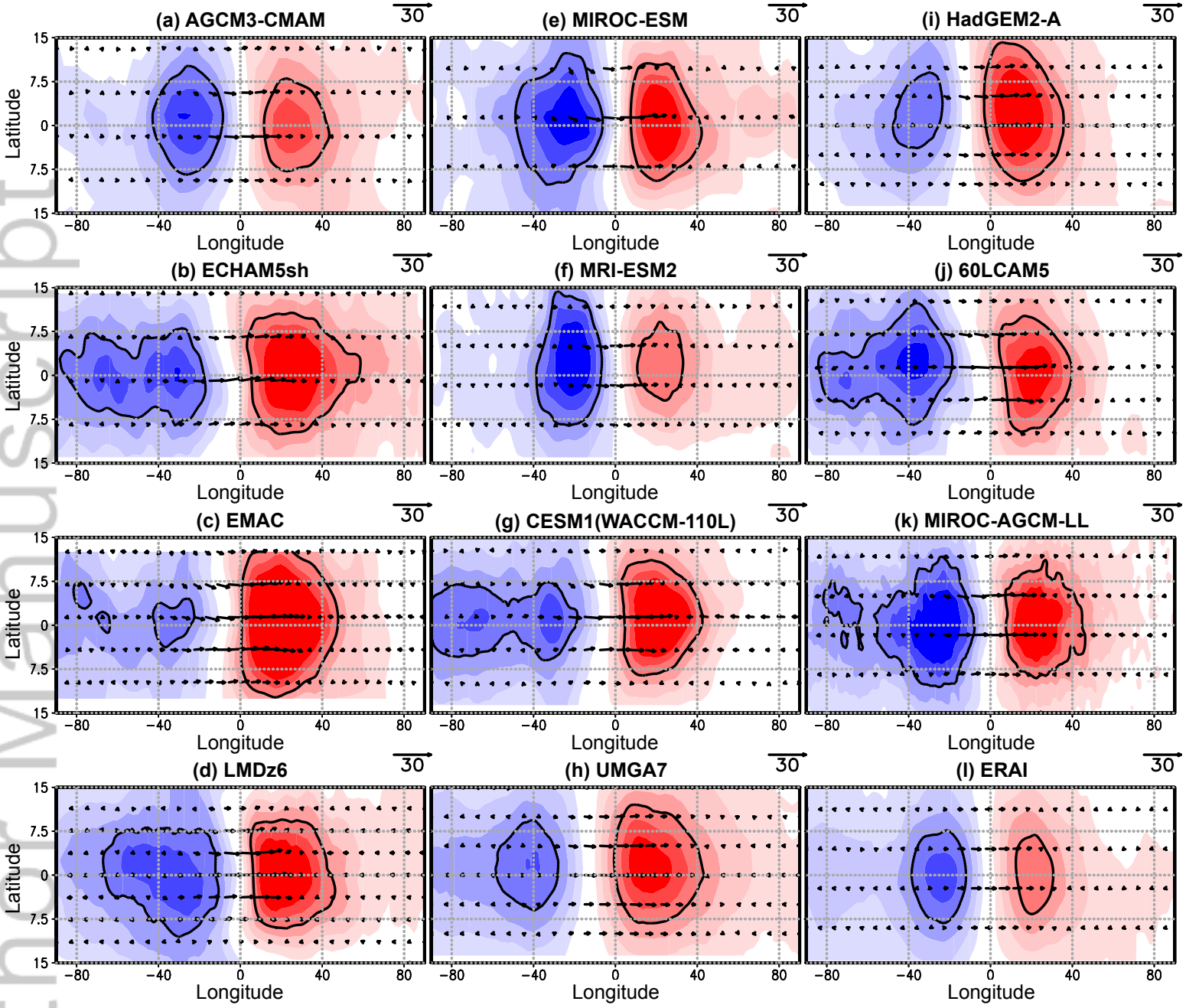

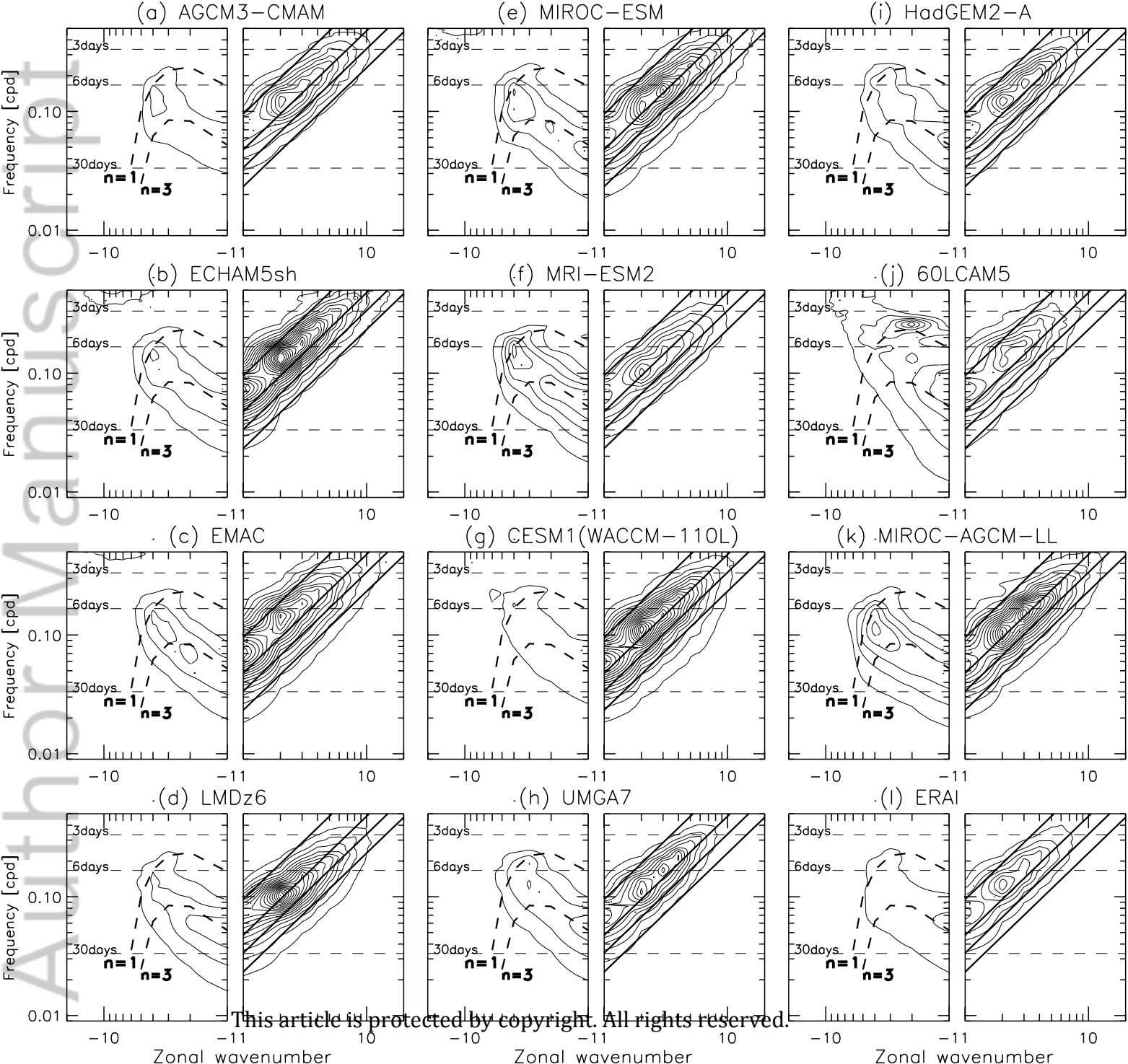

An evaluation of tropical waves and wave forcing of the QBO in the QBOi models

Holt, L. A., Lott, F., Garcia, R., Kiladis, G. N., Anstey, J., Braesicke, P., Bushell, A., Butchart, N., Cagnazzo, C., Chen, C.-C., Chun, H.-Y., Hamilton, K., Kawatani, Y., Kerzenmacher, T., Kim, Y.-H., McLandress, C., Naoe, H., Osprey, S., Richter, J., Scinocca, J., Serva, F., Versick, S., Watanabe, S., Yoshida, K. and Yukimoto, S.

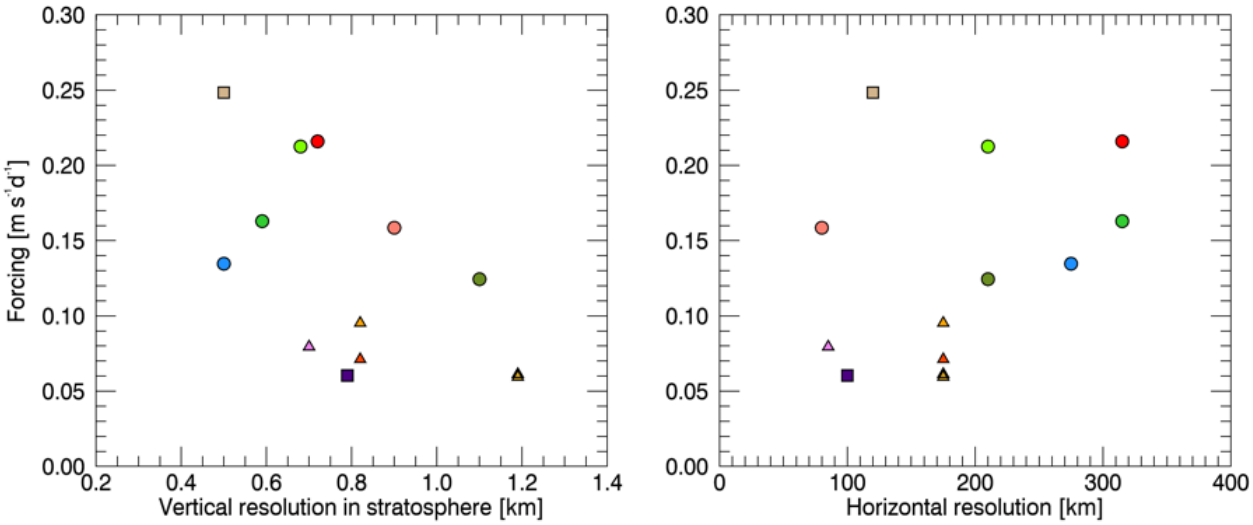

The QBOi models vary widely in their ability to simulate equatorial waves and in the magnitude of resolved wave-forcing contributing to the driving of the model QBO. In the QBOi models, despite the varying setups, vertical resolution emerged as a clear factor controlling the degree of wave forcing in the eastward QBO shear zones.
This figure shows how the wave forcing due to resolved large-scale eastward propagating waves relates to model vertical and horizontal resolution.